

# The Effects of Wind Farm Wakes on Freezing Sea Spray in the Mid-Atlantic Offshore Wind Energy Areas

David Rosencrans<sup>1,2</sup>, Julie K. Lundquist<sup>1,2,3</sup>, Mike Optis<sup>2,4</sup>, and Nicola Bodini<sup>2</sup>

<sup>1</sup>Department of Atmospheric and Oceanic Sciences, University of Colorado, Boulder, 80303, USA

<sup>2</sup>National Renewable Energy Laboratory, Golden, 80401, USA

<sup>3</sup>Renewable and Sustainable Energy Institute, Boulder, 80303, USA

<sup>4</sup>Veer Renewables, Courtenay, V9N 9B4, Canada

*Correspondence to:* David Rosencrans (David.Rosencrans@Colorado.edu)

## Abstract

The U.S. is expanding its wind energy fleet offshore where winds tend to be strong and consistent. In the mid-Atlantic, strong winds, which promote convective heat transfer and wind-generated sea spray, paired with cold temperatures can cause ice on equipment when plentiful moisture is available. Near-surface icing is induced by a moisture flux from sea spray, which poses a risk to vessels and crews. Ice accretion on turbine rotors and blades occurs from precipitation and in-cloud icing at temperatures below freezing. Ice accretion induces load and fatigue on mechanical parts which reduces blade performance and power production. Thus, it is crucial to understand the icing hazard across the mid-Atlantic. We analyze Weather Research and Forecasting model numerical weather prediction simulations at coarse temporal resolution over a 21-year period to assess freezing events over the long-term record and at finer granularity over the 2019–2020 winter season to identify the post-construction turbine impacts. Over the 2019–2020 winter season, results suggest that sea-spray–induced icing can occur up to 67 hours per month at 10 m at higher latitudes. Icing events during this season typically occur during cold air outbreaks (CAO), which are the introduction of cold continental air over the warmer maritime surface. During the 2019–2020 winter season, CAO lasted a total duration of 202 hours. While not all FSS events occurred during CAO over the 21 year period, all CAO events had FSS present. Further, we assess the turbine–atmosphere impacts of wind plant installation on icing using the fine-scale simulation data set. Wakes from large wind plants reduce the wind speed which mitigates the initiation of sea spray off white-capped waves. Conversely, the near-surface turbine-induced introduction of cold air in frequent wintertime unstable conditions enhances the risk for freezing. Overall, the turbine–atmosphere interaction causes a small reduction of FSS hours within the wind plant areas, with a reduction up to 15 hours in January at the 10 and 20 m heights.

## 1 Introduction

The offshore wind energy industry is undergoing rapid growth to supply emissions-free energy to the electrical grid. In the U.S., offshore capacity targets are approaching 40 GW by 2040 (Musial et al., 2022). Capacity expansion into relatively cold offshore regions will subject turbines to harsher wintertime conditions, which necessitate an understanding of the hazards that marine icing poses to offshore wind turbines, service vessels, and crew safety.

38

39 Ice accretion reduces the aerodynamic efficiency of the turbine blade, which hinders energy capture and annual  
40 energy production (Battisti et al., 2006; Kraj and Bibeau, 2010; Wei et al., 2020). Ice can remain on the rotors even  
41 after freezing conditions end, as slow natural processes such as ice shedding and melting extend the limitation to  
42 energy yield (Gao and Hong, 2021). One study found that excessive icing induced a power loss of 63 % for a single  
43 turbine over a 51-h icing event (Gao and Hu, 2021). Faster winds during cold front passages can enhance wind-  
44 energy supply during high-load cold-weather events, although, following frontal passages, the combination of cold  
45 temperatures and slow wind speeds may pose severe challenges for utility grid planners (Novacheck et al., 2021).  
46 Despite the energy losses from ice accretion, various strategies can mitigate or even prevent ice accretion altogether  
47 (IEA, 2018; Madi et al., 2019). While turbine blade icing is well studied (IEA, 2018; Martini et al., 2021; Contreras  
48 Montoya et al., 2022), icing near the turbine base, affecting operations and maintenance activities, is not.

49

50 The leading causes for low-level offshore icing are wave-impact and wind-induced sea spray (Dehghani-Sanij et  
51 al., 2017). Sea spray provides nuclei for ice clouds at high latitudes where airborne dust is sparse, being lofted by  
52 bursting bubbles and droplets from white-capped waves (Russell, 2015; Dehghani-Sanij et al., 2017). Ice  
53 accumulation from spray raises the center of gravity of ships, which can cause loss of stability and lead to capsizing  
54 (Guest and Luke, 2005). Observations suggest that the liquid droplets torn off of white caps, referred to as spume,  
55 experience a marked increase in concentration with strong winds above  $9 \text{ m s}^{-1}$  (Ross and Cardone, 1974; Monahan  
56 et al., 1983; Monahan and MacNiocaill, 1986). Further, spray particles more easily supercool with cold sea surface  
57 temperatures (SST) below  $7^\circ \text{ C}$  and at air temperatures below the freezing point for saline ocean water at  $-1.7^\circ \text{ C}$   
58 (U.S. Navy, 1988; Guest and Luke, 2005). Ice accumulation is believed to have caused the recent losses of three  
59 ships, including 1) the *Destination*, which sank near St. George Island, Alaska in 2017 (Kraegel, 2018); 2) the  
60 *Scandies Rose*, which sank southeast of Kodiak, Alaska, in 2019 (NTSB, 2021); and 3) the *Onega*, which sank in the  
61 Barents Sea in 2020 (Nilsen, 2020). To mitigate ice-induced accidents, inclement weather forecasts are furnished for  
62 coastal waters. A Coastal Waters Forecast, delivered by the National Weather Service, will contain a “freezing spray  
63 advisory” if freezing water droplets can accumulate on vessels due to a combination of SST, wind speed, air  
64 temperature, and vessel motion (Glossary - NOAA’s National Weather Service, 2023). At accumulation rates greater  
65 than  $2 \text{ cm h}^{-1}$ , the advisory becomes a “heavy freezing spray watch”.

66

67 Wind turbines can modify the amount and severity of icing conditions via competing effects. Enhanced  
68 turbulence caused by spinning blades transports heat from aloft to lower altitudes within the rotor-swept region or  
69 near the surface. In stable stratification, warmer potential temperatures are transported downward, which introduces  
70 a near-surface warming effect, and vice versa in unstable conditions (Fitch et al., 2013; Rajewski et al., 2013; Xia et  
71 al., 2016; Siedersleben et al., 2018; Tomaszewski and Lundquist, 2020). However, recent research suggests taller  
72 turbines may reverse this phenomenon (Golbazi et al., 2022) depending on the depth of the atmospheric boundary  
73 layer (Quint et al., 2024). As the winter months feature more frequent unstable stratification along the U.S. East  
74 Coast (Bodini et al., 2019), turbine-induced cooling may increase the potential for near-surface freezing. In contrast,

75 turbines harness momentum from the flow, which reduces the downwind wind speed (Nygaard, 2014; Platis et al.,  
76 2018; Schneemann et al., 2020). A reduction in wind speed conversely reduces the potential for icing (Dehghani-  
77 Sanij et al., 2017). Thus, it is crucial to understand how large-scale wind deployment across the mid-Atlantic will  
78 modify the regularity and intensity of freezing sea spray (FSS) conditions.

79

80 Herein, we employ numerical weather prediction modeling to quantify the baseline offshore icing risk and the  
81 wind plant post-construction effects. Section 2 outlines the modeling setup and discusses the techniques for  
82 discerning icing conditions and cold air outbreak events. Section 3 reports results for the spatiotemporal icing risk,  
83 causal factors, and the adjustments by wind plants. Section 4 offers concluding remarks and discussion.

84

## 85 **2 Methods**

### 86 **2.1 NOW-23**

87 We explore annual variability of FSS conditions using the 2023 National Offshore Wind (NOW-23) data set  
88 (NREL, 2020; Bodini et al., 2024). This data set quantifies wind resources spanning all offshore regions of the  
89 United States for more than 20 years using the Weather Research and Forecasting (WRF) model version 4.2.1  
90 (Powers et al., 2017). We acquire model output at an hourly temporal resolution for the 21-year period from 01  
91 January 2000 to 31 December 2020. A parent domain feeds into an inner nested domain with horizontal grid  
92 resolutions of 6 km and 2 km, respectively. Both domains incorporate a vertical grid resolution of 5 m near the  
93 surface with stretching to 45 m aloft, using 61 vertical levels up to a 50 hPa top. The European Centre for Medium  
94 Range Weather Forecasts 5 Reanalysis (ERA5) dataset supplies hourly initial and boundary conditions at a 30 km  
95 resolution to WRF (Hersbach et al., 2020). NOW-23 employs the MYNN2 planetary boundary layer and surface  
96 layer (Nakanishi and Niino, 2006) schemes, eta microphysics (Ferrier et al., 2002), the Noah Land Surface Model  
97 (Tewari et al., 2004), the rapid radiative transfer model for shortwave and longwave radiation (Iacono et al., 2008),  
98 and the Kain–Fritsch cumulus parameterization (Kain, 2004) in the outmost domain only. For the mid-Atlantic  
99 region, NOW-23 was validated against observations from three ZephIR ZX300M floating lidars (Pronk et al., 2022).

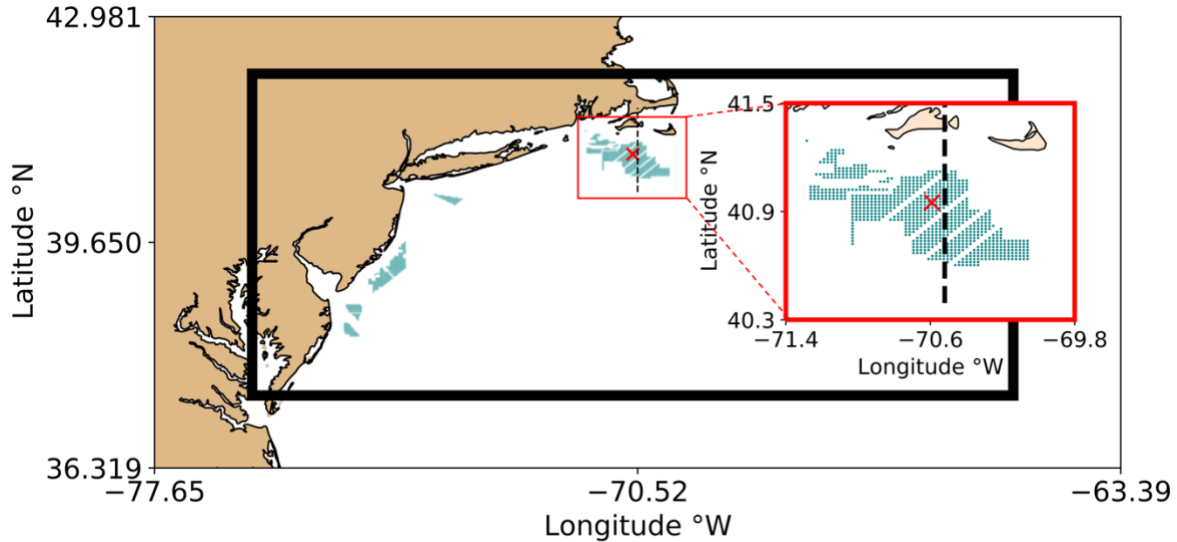
100

101

### **2.2 NOW-WAKES**

102 We explore the seasonal variability and impacts of wind plants on icing conditions using high-fidelity numerical  
103 weather prediction simulations over the period 01 September 2019 to 31 August 2020. These validated WRF version  
104 4.2.1 simulations are described in detail in Rosencrans et al., (2024) but are summarized here for the reader's  
105 convenience. This period is chosen for the availability of lidar measurements for validation of the wind speed  
106 profile. A parent domain hosts an inner nest with horizontal grid resolutions of 6 km and 2 km, respectively (Figure  
107 1). Both domains include a vertical grid resolution of 10 m near the surface with stretching aloft, using 54 vertical  
108 levels up to a 50 hPa top. The inner domain outputs data at an instantaneous history file frequency of 10 minutes.  
109 Constant time steps are set to 18 s and 6 s in the outer and inner domains, respectively. Initial and boundary  
110 conditions are also supplied by the hourly 30 km ERA5 dataset (Hersbach et al., 2020). Lower boundary conditions  
111 are provided as SST by the UK Met Office Operational Sea Surface Temperature and Sea Ice Analysis dataset  
112 (Donlon et al., 2012) and show good agreement during validation against mid-Atlantic bight buoys (Redfern et al.,

113 2023). Physics parameterizations include the MYNN2 planetary boundary layer and surface layer (Nakanishi and  
 114 Niino, 2006), the Noah Land Surface Model (Niu et al., 2011), the New Thompson microphysics (Thompson et al.,  
 115 2008), the rapid radiative transfer model for longwave and shortwave radiative transfer (Iacono et al., 2008), and the  
 116 Kain–Fritsch Cumulus (Kain, 2004) schemes. The Kain–Fritsch cumulus parameterization applies to the parent  
 117 domain only. We incorporate spectral nudging to relax model output toward the ERA5 boundary conditions in the  
 118 inner domain. We apply a cutoff wavenumber of 3 (Gómez and Miguez-Macho, 2017), above which model  
 119 dynamics may resolve freely. No nudging is applied beneath the boundary layer height.  
 120



121  
 122 **Figure 1. Modeling domains.** The entirety of the outer domain with inner domain is shown, outlined by the black  
 123 rectangle. The red square is zoomed in on the Rhode Island–Massachusetts (RIMA) block to enhance visibility. Turbines  
 124 are shown as teal dots. The red “X” indicates the point of interest (POI) where time series are acquired. The dashed black  
 125 line is a cross section extending through the RIMA block.

126  
 127 We incorporate the effects of wind turbines using the WRF wind farm parameterization (WFP) (Fitch et al.,  
 128 2012). WFP simulations feature wind plant layouts of the lease areas and include 1,418 turbines (Figure 1, Table 1).  
 129 The WFP incorporates the effects of turbines by implementing a drag-induced deceleration of wind flow and an  
 130 addition of turbulence at model levels intersecting the rotor area. We execute WFP simulations adding both 0 % and  
 131 100 % turbulent kinetic energy (TKE) (Rosencrans et al., 2024), although a smaller value of 25 % in some cases  
 132 agrees better with neutrally stratified large-eddy simulations (Archer et al., 2020). Differences in the number of icing  
 133 hours between 0 % and 100 % added TKE are slight, so we report those from 100 % added TKE only. Thus, for the  
 134 remainder of this article we refer to the 100 % added TKE simulation as “WFP”. This work utilizes 12 MW GE  
 135 Haliade wind turbines with a 138 m hub height and 215 m rotor diameter, which are scaled by Beiter et al. (2020)  
 136 from a 15 MW reference turbine. We carry out separate simulations using both no wind farms (NWF) and wind  
 137 farms (WFP) for the full year-long period from 01 September 2019 to 31 August 2020 (Table 1).  
 138

139  
140

**Table 1. List of NOW-WAKES WRF simulations characterized by turbine characteristics. The simulation period spans 01 September 2019 to 01 September 2020.**

Simulation type	Acronym	Turbine rated power	Added TKE	# Turbines
No Wind Farms	NWF	N/A	N/A	0
Wind Farm Parameterization	WFP	12 MW	100 %	1,418

141

### 2.3 Icing hours detection

142 Ice accretion occurs when supercooled water freezes upon contact with objects. The largest contributions to sea  
143 spray icing are provided by the bursting of bubbles and advection of spray from white-capped waves (Dehghani-  
144 Sanij et al., 2017). In the presence of moisture, three key variables dictate offshore freezing conditions: wind speed,  
145 SST, and air temperature (Overland et al., 1986; Overland, 1990; Guest and Luke, 2005; Dehghani-Sanij et al.,  
146 2017; Line et al., 2022).

147

148 We detect FSS conditions following common thresholds defined by the latter studies (Guest and Luke, 2005;  
149 Dehghani-Sanij et al., 2017; Line et al., 2022). These criteria require 1) wind speeds in excess of  $9 \text{ m s}^{-1}$ , 2) air  
150 temperatures below  $-1.7^\circ \text{ C}$ , and 3) SST less than  $7^\circ \text{ C}$ . Air temperature and SST thresholds can range between  $-2^\circ$   
151  $\text{C}$  and  $-1.7^\circ \text{ C}$  and between  $5^\circ \text{ C}$  to  $8.9^\circ \text{ C}$ , respectively, as reviewed by Dehghani-Sanij et al., (2017). As such, we  
152 provide a sensitivity assessment for the full range (Appendix B). The surface skin temperature (WRF output variable  
153 “TSK”) is assessed because the SST field inherits coarse blocks of missing data around coastlines from the ERA5  
154 dataset. The resulting spatial maps are masked by the land use (WRF output variable “LU\_INDEX”) to ensure that  
155 icing conditions over land are not counted. The number of 10 min timestamps where these criteria are met each  
156 month are recorded for all simulations. As sea spray often lofts to between 5 and 20 m above sea level (Dehghani-  
157 Sanij et al., 2017), we quantify sea spray-induced icing at the 10 and at 20 m heights. For the 20 m conditions, we  
158 use 20 m air temperatures but use 10 m wind speeds as those winds have been linked to the generation of spray off  
159 white-capped waves (Dehghani-Sanij et al., 2017; Guest and Luke, 2005; Line et al., 2022; Ross and Cardone, 1974;  
160 Monahan et al., 1983; Monahan and MacNiocaill, 1986).

161

162 Due to the height constraint of sea spray particles, we consider both precipitation-based and in-cloud icing at the  
163 138 m hub height by assessing different criteria for 1) the nonzero presence of liquid rain water (WRF variable  
164 “QRAIN”) that may become supercooled at temperatures less than  $0^\circ \text{ C}$ , 2) ice (WRF variable “QICE”), and 3) the  
165 aggregation from snow (WRF variable “QSNOW”) (Parent and Ilinca, 2011; ISO, 2017). Further, we detect cloud or  
166 fog formation when 4) the relative humidity (RH) is greater than or equal to 100% following:  
167

168

$$e_s = e_0 \exp \left[ \frac{b(T - T_1)}{(T - T_2)} \right] \quad (1)$$

169

$$w_s = \frac{\epsilon e_s}{p - e_s} \quad (2)$$

170 
$$RH = \frac{w}{w_s} \times 100\% \quad (3)$$

171 where  $e_s$  is the saturation mixing ratio,  $e_0$  is 6.112 mb,  $b$  is 17.67,  $T_1$  is 273.15 K,  $T_2$  is 29.65 K,  $T$  is the air  
 172 temperature,  $\epsilon$  is 0.622,  $p$  is the atmospheric pressure, and  $w$  is the mixing ratio (WRF output “QVAPOR”) (Stull  
 173 B., 1988). None of the aforementioned criteria must occur at the same time for icing to occur. However, we require  
 174 that one must occur in conjunction with an air temperature less than 0° C for an icing event.

175

176 **2.4 Ice accumulation rate**

177 A predictability function assesses the likelihood for freezing in the presence of sea spray. We assess the  
 178 predictability of icing conditions at the point of interest (POI) in the Rhode Island/Massachusetts (RIMA) block  
 179 (Figure 1) separately from the NOW-WAKES and the NOW-23 datasets. The predictability ( $PR$ ) for sea spray–  
 180 induced ice formation follows:

181 
$$PR = \frac{V_a(T_f - T_a)}{1 + 0.4(T_s - T_f)} \quad (4)$$

182 where  $V_a$  is the wind speed,  $T_f$  is the temperature threshold of  $-1.7^\circ$  C,  $T_a$  is the air temperature, and  $T_s$  is the SST  
 183 (Guest and Luke, 2005; Overland et al., 1986; Overland, 1990). A humidity variable is not present in Eq. (4) due to  
 184 the assumption that sea spray introduces a constant source of moisture during fast winds. A group of successive  
 185 timestamps with nonzero  $PR$  are considered the same event. Separate flagged timestamps occurring within 24 hours  
 186 of each other span the same synoptic regime (Winters et al., 2019), and so the entire duration between the two  
 187 flagged timestamps is considered one event. We additionally tested a threshold of 72 hours to account for synoptic  
 188 conditions spanning a longer duration but found that one FSS event lasted for over a week and our three FSS criteria  
 189 were only met 8 % of the time during the event. As such, the 72-h threshold was not justified.

190

191 **Table 2. Icing rate by PR. Rows delineate the PR value, icing class, and ice accretion rate. Columns delineate the icing**  
 192 **rate per PR range. From Guest and Luke (2005).**

PR	<0	0–22.4	22.4–53.3	53.3–83.0	>83.0
Icing Class	None	Light	Moderate	Heavy	Extreme
Icing Rate [cm h <sup>-1</sup> ]	0	<0.7	0.7–2.0	2.0–4.0	>4.0

193

194 The magnitude of  $PR$  can determine the rate of ice accretion (Table 2). The ice accretion rates are a general  
 195 guideline developed for 20 to 75 m long vessels; specific rates depend on the type of ship, its load, heading relative  
 196 to the prevailing wind direction, and its handling characteristics (U.S. Navy, 1988; Guest and Luke, 2005). For  
 197 instance, a larger ship requires faster winds and taller waves for sea-spray–induced ice to accumulate on a higher  
 198 deck but is more vulnerable to the prevailing wind direction due to reduced maneuverability. It is not known how  
 199 these icing rates would apply to wind turbines or to the vehicles used to access offshore wind turbines.

200

## 2.5 Cold air outbreak detection

Freezing conditions can be stimulated by the advection of cold continental air over a warmer maritime surface. The resulting temperature profile causes thermal instability, which can induce filamentary convective rolls that align to make cloud “streets” with parallel columns of ascending and descending air that transform into open convective cells further offshore (Geerts et al., 2022). Convective rolls can be used to identify cold air outbreak (CAO) (Atkinson and Wu Zhang, 1996; Geerts et al., 2022) and may also contribute moisture for in-cloud icing if the lifting condensation level is at or below rotor-swept heights. A quantitative approach proposed by Vavrus et al. (2006) identifies a cold air outbreak (CAO) by the magnitude and duration of anomalous air temperature, which we apply at the POI (Figure 1). This strategy requires that the near-surface temperature be at least 2 standard deviations below the wintertime average following Eq. (5):

$$T < \bar{T} - 2(\sigma) \quad (5)$$

where  $T$  is the 2 m temperature,  $\bar{T}$  is the average 10 m temperature over the entire wintertime period, and  $\sigma$  is the standard deviation. The wintertime period spans November through March at a 10 min frequency to account for all non-zero-freezing predictability events. Again, successive timestamps with detected CAO are considered a single event, and separate events occurring within a 24 h span are conglomerated into the same event.

## 2.6 Atmospheric stability

Turbulence from wind turbines modifies the near-surface temperature based on the atmospheric stability or stratification. We calculate the modeled atmospheric stability using the Obukhov Length ( $L$ ) (Monin and Obukhov, 1954) (Eq. 6), which delineates the height above the surface at which buoyant turbulence equals mechanical shear production of turbulence, at a point centered on the RIMA block of lease areas:

$$L = -\frac{u_*^3 \overline{\theta_v}}{\kappa g \overline{w' \theta_v'}} \quad (6)$$

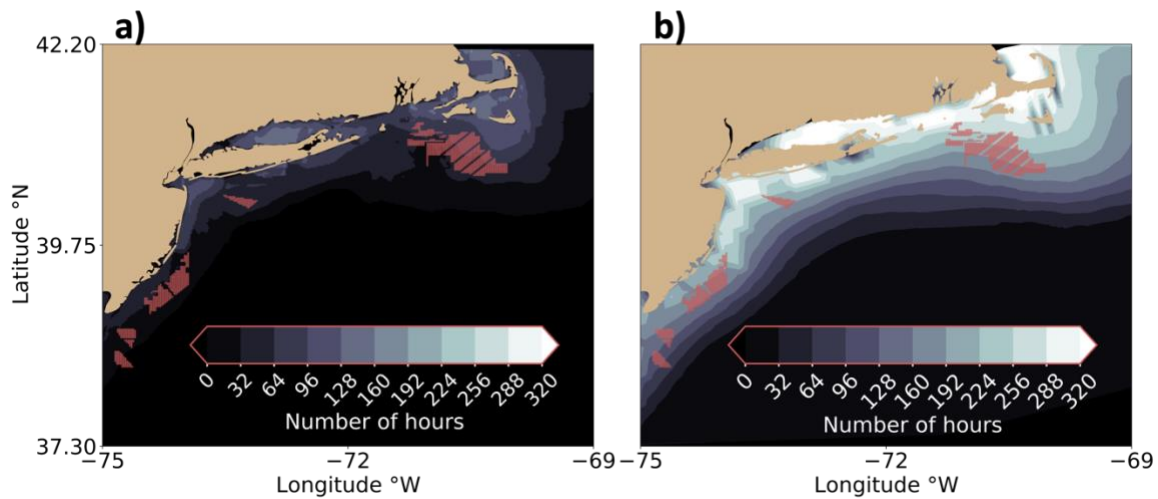
where  $u_*$  (UST in WRF output) is the friction velocity,  $\theta_v$  is the virtual potential temperature,  $\kappa$  is the von Kármán constant of 0.4,  $g$  is gravitational acceleration of  $9.81 \text{ m s}^{-1}$ , and  $\overline{w' \theta_v'}$  (HFX in WRF output) is the surface dynamic heat flux converted into kinematic heat flux. Negative lengths between 0 m and  $-500$  m imply unstable stratification due to a positive heat flux (Gryning et al., 2007; Archer et al., 2016). Conversely, lengths between 0 m and 500 m imply stable stratification due to a negative heat flux. Lengths approaching negative or positive infinity imply neutral stratification, as buoyancy is no longer a dominating factor. Each 10 min timestamp from the NWF run is assigned a stability classification from November 2019 to March 2020.

# 3 Results

## 3.1 Spatial variability of icing conditions

The prevalence of icing conditions exhibits regional variability. The commonality of icing increases toward higher latitudes and near the coast where cold continental air advects over the ocean during the winter (Figure 2). In general, the spatial icing pattern during the 2019–2020 winter season (Figure 2a) matches well with the pattern over the 21-year period (Figure 2b) although the 2019–2020 season is relatively mild compared to other winters (Figure 2, Figure 3a). Icing conditions shadow the mid-Atlantic coast but occur less often along the New Jersey Bight where

238 wind speeds decrease and air and sea temperatures warm. The prevalence of freezing conditions extends furthest  
 239 offshore southeast of Nantucket and enhances in the Long Island Sound; both regions feature local minima in mean  
 240 January 2020 SST less than 5° C. The Long Island Sound is flanked by land to the north and south which amplifies  
 241 the presence of cold air. In addition, mean wind speeds maximize to the east of Cape Cod and Nantucket (Bodini et  
 242 al., 2024) which increases the number of hours that wind-generated spray is present. Finally, the cyclonic current in  
 243 the Gulf of Maine transports water southward. East of Cape Cod, this current bifurcates around the Georges Bank,  
 244 and a branch feeds cold water into the mid-Atlantic (Chapman et al., 1986). The number of icing hours may be  
 245 further exacerbated when predominant northerly winter winds instigate onshore Ekman transport toward the coast,  
 246 which is favorable for downwelling (Shcherbina and Gawarkiewicz, 2008b). However, downwelling is not always  
 247 supported, as the mixed layer stratification is dominated by salinity (Shcherbina and Gawarkiewicz, 2008a), leaving  
 248 a cold pool near the surface.  
 249



250  
 251 **Figure 2. The number of hours FSS conditions occur at 10 m during (a) the November 2019 to March 2020 period in**  
 252 **NWF and (b) the mean November to March period from 2000 to 2020 in NOW-23. Lighter contouring indicates more**  
 253 **freezing hours. Red dots represent turbine locations but do not exist in (a) or (b) and are shown for reference.**

254  
 255  
 256  
 257 Icing conditions exhibit seasonal variability in NWF, starting at 0 hours in November, increasing through the  
 258 winter, and falling to 0 again by April at all heights (Figure 3 and Figure. A1–A3). At the 10 m altitude, FSS  
 259 conditions occur most often in January, up to 67 hours, with an offshore spatial extent of 59,292 km<sup>2</sup>, or 12.3 times  
 260 the area of the wind plants. At 20 m, FSS conditions also occur most often in January, up to 68 hours, covering a  
 261 total area of 61,736 km<sup>2</sup>, or roughly 12.8 times the area of the wind plants (Figure A2). The 138 m hub height attains  
 262 the largest maximum of 119 hours during January in the Gulf of Maine and to the east Cape Cod (Figure A3), with  
 263 an offshore spatial extent of 291,012 km<sup>2</sup>, or 60.2 times the area of the wind plants.  
 264



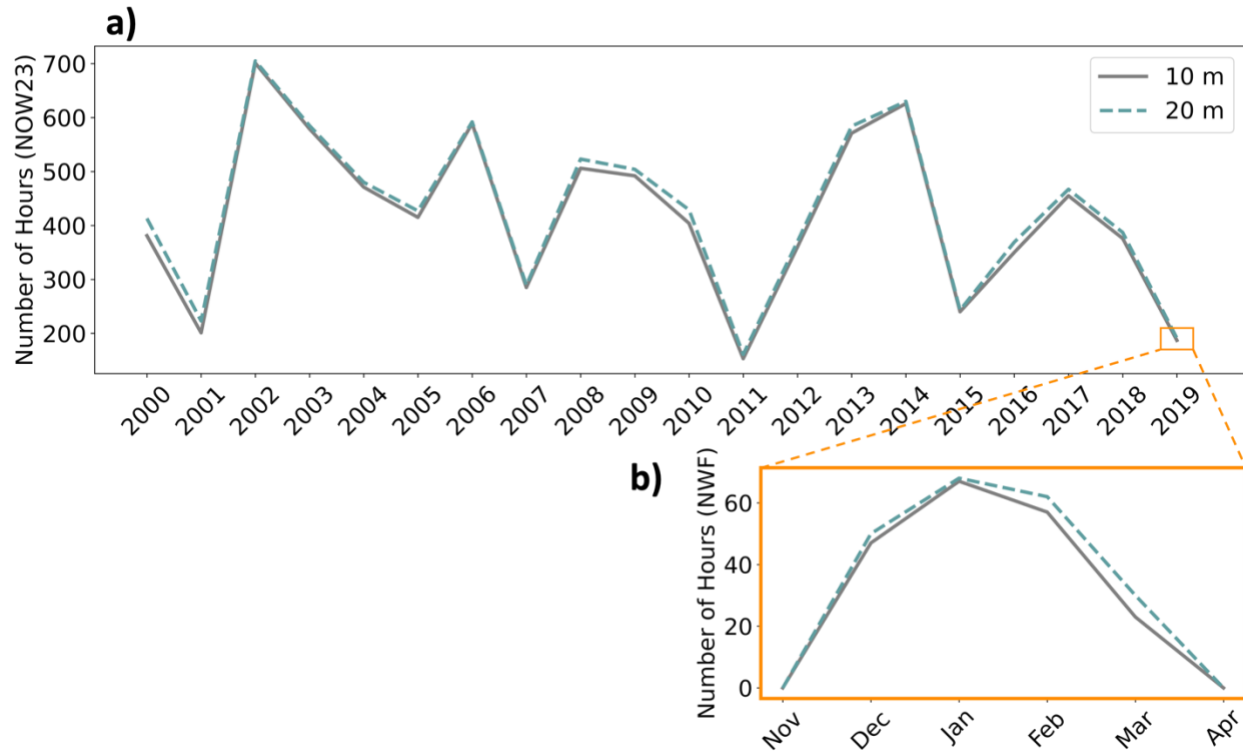


**Figure 3. The maximum number of FSS hours over the OCS (a) annually and (b) seasonally in NOW-23. The zoomed orange cutout shows the seasonal variation over the 2019–2020 winter.**

265  
266  
267

268

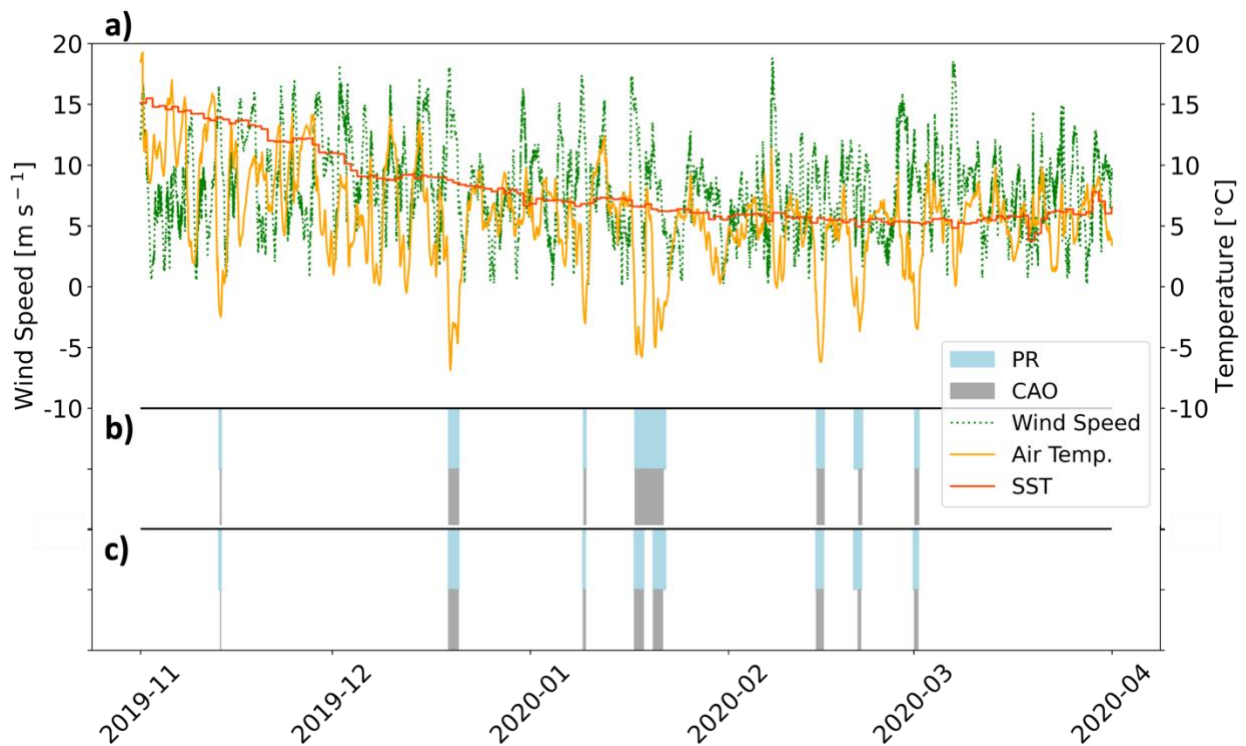
269 The 2019–2020 winter season was one of the mildest compared to other winters (Figure 3a), as assessed using  
270 the FSS detection criteria (Section 2.3). This winter season had few icing hours compared to other winters over the  
271 21-year period, reaching 194 hours in NWF or 187 hours in NOW-23 at 10 m. At 20 m, the 2019–2020 winter  
272 season contains 210 hours in NWF or 191 hours in NOW-23. The greatest number of icing hours occurs during the  
273 2002–2003 season, with 701 total hours at 10 m and 705 hours at 20 m. While the 21-year slope shows a decrease, it  
274 is not statistically significant using the Mann–Kendall (M–K) test (Hussain and Mahmud, 2019). P-values for the  
275 maximum number of icing hours (found across the OCS) (Figure 3a) and for the number of hours at the POI (Figure  
276 1) are 0.20 and 0.12, respectively. We additionally applied the seasonal M–K test (Hirsch et al., 1982) to account for  
277 upward and downward trends throughout the year on monthly mean PR, monthly maximum PR, and the monthly  
278 total number of icing hours at the POI. Neither test returned a statistically significant trend.

279

### 280 3.2 Icing conditions and cold air outbreak

281 Investigating all events with a non-zero PR at the POI (Figure 1) reveals similar synoptic trends. We identify  
282 seven events with FSS conditions with a total duration of 253 hours from November 2019 to March 2020. All times  
283 during the 2019–2020 winter period with nonzero PR contain light ice accumulation of less than  $0.7 \text{ cm h}^{-1}$  (Table  
284 2). During each FSS event, higher relative pressure resided to the southwest throughout the Great Plains,  
285 Appalachia, or the Great Lakes with lower relative pressure to the northeast around Nova Scotia and

286 Newfoundland. In the Northern Hemisphere, winds flow with higher pressure to the right and lower pressure to the  
 287 left (Wallace and Hobbs, 2006). This flow regime results from the balance between the pressure gradient force and  
 288 the Coriolis force, which is a force introduced into the equations of motion to account for acceleration on a non-  
 289 inertial rotating reference frame (Ferrel, 1856). The largest pressure gradient forces occurred during the two January  
 290 events reaching 4 hPa per 100 km, or roughly 4 times the pressure gradient force required for a  $10 \text{ m s}^{-1}$  geostrophic  
 291 wind in the midlatitudes. Most events feature a cold front in the mid-Atlantic. This pressure regime directs quasi-  
 292 geostrophic flow near the surface toward the southeast, introducing cold continental air offshore. During the winter,  
 293 the prevailing wind direction is northwesterly across the mid-Atlantic OCS (Bodini et al., 2019) because regions of  
 294 land mass feature higher surface pressure than the surrounding ocean and the Bermuda High retreats to the east.  
 295



296  
 297 **Figure 4. (a) Time series of wind speed (green dotted), 10 m air temperature (orange), and SST (red) from November**  
 298 **2019 to April 2020 at the downwind edge of Vineyard Wind (Figure 1). Light-blue shading indicates the duration of**  
 299 **nonzero PR, and gray shading indicates the duration of detected CAO from (b) NWF and (c) NOW-23.**

300  
 301 All FSS events, assessed using PR, coincide with CAO. We detect seven CAO events in NWF with a total  
 302 duration of 202 hours (Figure 4b). The mean duration of CAO events (29 hours) are seven hours shorter than FSS  
 303 events (36 hours), with 80 % of flagged FSS timestamps having CAO present.

304  
 305 Common between events are fast wind speeds and cold 10 m air temperatures; SST plays a secondary role for  
 306 its weak temporal variability (Figure 4a). The average wind speed during FSS events is  $10 \text{ m s}^{-1}$  with gusts

307 exceeding  $15 \text{ m s}^{-1}$  during four events. Nonzero PR does not occur until after the wind speed peaks, when cold air  
308 temperatures sweep in, averaging minimum temperatures of  $-4.5^\circ \text{ C}$  (Figure 4a). This wind speed–temperature  
309 dynamic can pose a challenge for grid planners if wind energy generation reduces during periods of high demand for  
310 residential and commercial heating, especially in a future scenario with electrification of space heating.

311

312 During the 2019–2020 winter in the NOW-23 dataset, eight total events are flagged as candidates for FSS  
313 because the longest event in January 2020 (Figure 4b) is split among two separate events; all eight events have a  
314 corresponding CAO (Figure 4c). Over the 21-year period, *all* CAO events occur in conjunction with an FSS event  
315 (positive PR) (Fig. C1–Fig. C20). However, many FSS events occur without CAO present meaning that CAO is  
316 only one of the drivers, and large interannual variability can exist. For instance, while 100 % of CAO timestamps  
317 concur with FSS during the 2011–2012 season, only 10 % do during the 2013–2014 season.

318

319 The 2019–2020 winter ice accumulation rate is similar to other winters. The average PR during freezing events  
320 from 2019 to 2020 is 4.3, which corresponds to a light ice accumulation rate of less than  $0.7 \text{ cm h}^{-1}$  (Table 2). Over  
321 the 21-year period, the average PR among events is 8.1, which corresponds to the same accumulation rate. The  
322 2003–2004 winter period features the greatest mean PR of 15.7, which also corresponds to a light ice accumulation  
323 rate. During this winter, a moderate risk for icing occurred 18 % of the time, and a heavy risk occurred 3 % of the  
324 time, corresponding with icing rates between  $0.7\text{--}2.0 \text{ cm h}^{-1}$  and  $2.0\text{--}4.0 \text{ cm h}^{-1}$ , respectively, and possibly  
325 triggering heavy freezing spray watches in the NWS advisory.

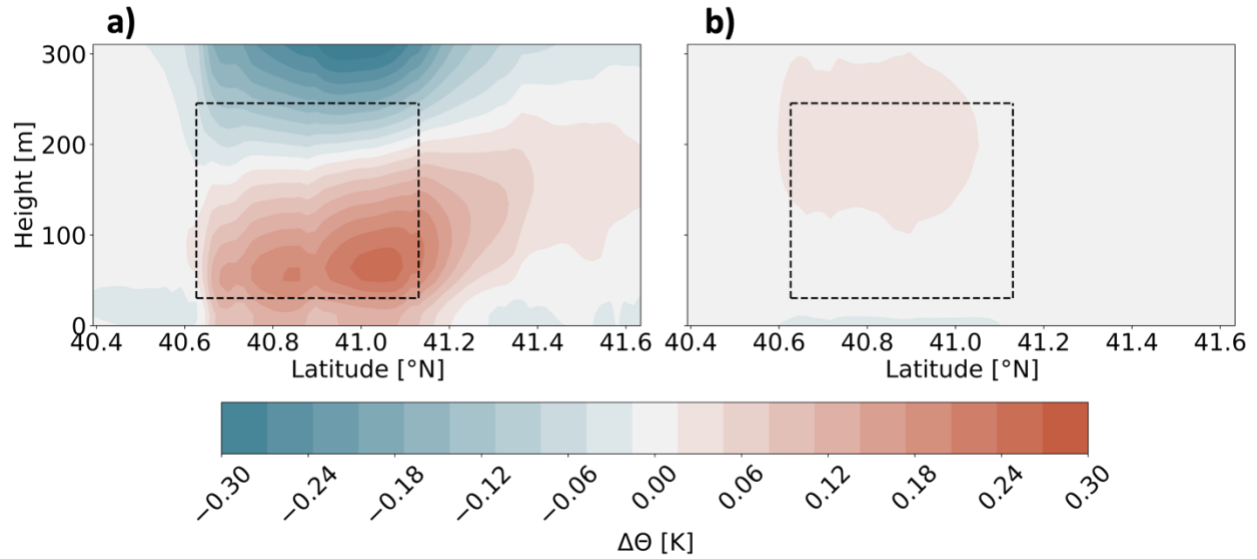
326 Synoptic-scale teleconnection patterns can impact the likelihood of icing conditions. From December 2003 to  
327 March 2004, the Pacific North Atlantic (PNA) cycle was positive. During the positive phase of PNA, a relative high-  
328 pressure anomaly with anticyclonic wind flow exists over the western US that is conducive to northwesterly  
329 transport of cold air over the East Coast (Vavrus et al., 2006). In addition, the entire November 2003 to March 2004  
330 period featured a positive El Niño-Southern Oscillation (ENSO) index. Positive ENSO has been attributed to cooler  
331 SSTs across the mid-Atlantic and northeasterly winds which advect cold air from the north (Alexander and Scott,  
332 2002). Other teleconnection patterns, including the Arctic Oscillation and North-Atlantic Oscillation switched signs  
333 during this winter and are not discussed in greater detail.

334

### 335 **3.3 Modifications by wind plants**

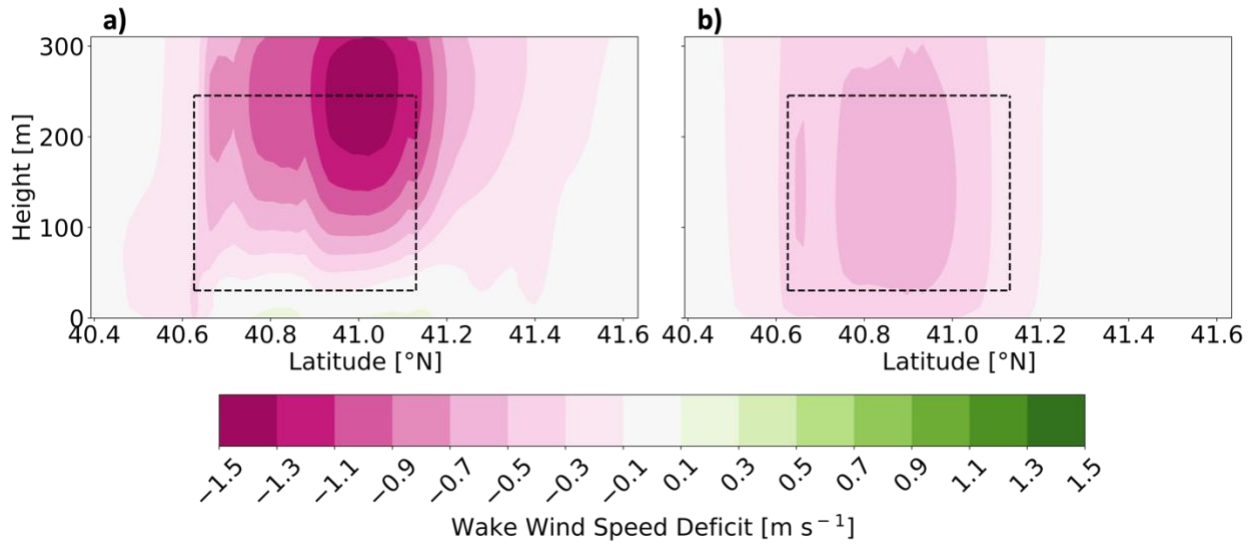
336 The near-surface cooling effect by rotor turbulence provides a subtle effect on freezing conditions. In unstable  
337 conditions, which occur 64 % of the time from November 2019 through March 2020 in NWF assessed at the POI,  
338 wind turbines introduce near-surface cooling, which could increase the likelihood of freezing. Mean cooling and  
339 warming during unstable conditions reach magnitudes up to  $-0.041 \text{ K}$  at the surface and  $0.022 \text{ K}$  within the rotor-  
340 swept region, respectively, along a cross section extending through the RIMA block (Figure 1, Figure 5b). During  
341 stable conditions, which occur 25 % of the time from November through March, cooling aloft reaches up to  $-0.34$   
342  $\text{K}$ , and near-surface warming reaches  $0.26 \text{ K}$  (Figure 5a). Near-surface cooling exists adjacent to the wind plant  
343 cluster (Xia et al., 2016).

344



345 **Figure 5. The mean (WFP-NWF) potential temperature difference during (a) stable stratification and (b) unstable**  
 346 **stratification, from November 2019 to March 2020. The cross section spans the RIMA block of lease areas (Figure 1). Red**  
 347 **contouring indicates warming, and blue indicates cooling. Dashed lines outline the wind plant area and rotor-swept**  
 348 **region.**  
 349

350  
 351 The reduction of wind speeds in the wake modifies the chance for icing within the rotor-swept area and near the  
 352 surface by reducing the production of white-capped waves and the wind-induced tearing of spray off waves. In  
 353 stable conditions, the mean wake wind speed deficit is largest, reaching  $-1.4 \text{ m s}^{-1}$  near the top of the rotor-swept  
 354 plane, reducing the chance for icing. Because vertical motion is suppressed in stable stratification, winds enhance  
 355 and flow around and under the wind plant area (Figure 6a), reaching a subtle enhancement near the surface of  $0.18$   
 356  $\text{m s}^{-1}$ . In unstable stratification, available buoyant turbulence promotes mixing which transports momentum from  
 357 above the rotor-swept region down to within the wake. The injection of momentum allows wake wind speeds to  
 358 recover, leaving a smaller maximum averaged wake deficit of  $-0.57 \text{ m s}^{-1}$  (Figure 6b). There is no enhancement of  
 359 wind speeds adjacent to the RIMA block along the cross section in unstable conditions.



361  
 362 **Figure 6. The mean (WFP-NWF) wind speed difference during (a) stable and (b) unstable stratification, from November**  
 363 **2019 to March 2020. The cross section spans the RIMA block of lease areas (Figure 1). Pink contouring indicates a wind**  
 364 **speed reduction, and green indicates wind speed enhancement. Dashed lines outline the wind plant area and rotor-swept**  
 365 **region. Note the very small enhancement of wind speeds near the surface in stable conditions.**

366  
 367 Despite near-surface cooling, net FSS conditions in WFP occur less often than in NWF when diagnosed using  
 368 wind speed, air temperature, and SST criteria because of the wake wind speed reduction. At 10 m, the turbine–  
 369 atmosphere interaction alters possible icing conditions the most in February, with a maximum reduction by 15 hours  
 370 (Table 3). At 20 m, wind plants cause a reduction by up to 15 hours in January and February. In each case, the  
 371 reduction in possible icing conditions is spatially coincident with the wind plant areas (Figure 7). At the 138 m hub  
 372 height, the change to the number of FSS hours also maximizes in January and February, with a reduction by 9 hours.

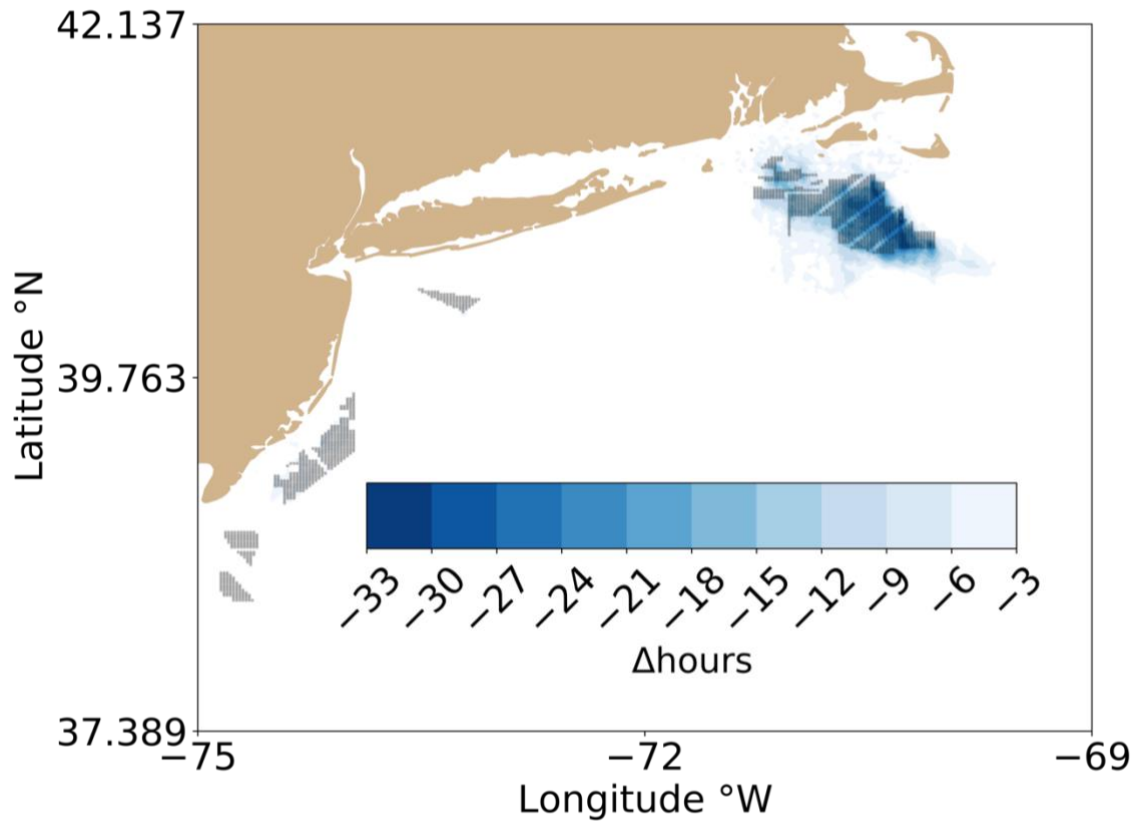
373

374

**Table 3. The maximum turbine-induced change in FSS hours by month and height.**

	November	December	January	February	March	April
10 m	0	-3	-14	-15	-11	0
20 m	0	-4	-15	-15	-12	0
138 m	0	-5	-9	-9	-5	0

375



377

378

379

**Figure 7. The (WFP-NWF) change in number of FSS hours at 10 m November 2019 to March 2020. Blue contours indicate a reduction.**

380

381

382

383

384

385

386

387

388

389

390

391

392

393

394

395

Similarly, the presence of wind turbines has a minimal impact to the number of hours FSS conditions occur by means of icing PR at the POI. The duration of nonzero PR over the November through March winter period increases by 3 hours, or from 253 to 256 hours total, at a point centered on the RIMA block. The total duration of CAO does not change after the installation of wind plants and remains at 202 hours. The total number of events (seven) does not change in the presence of wind turbines, and all flagged timestamps still cause light icing of less than  $0.7 \text{ cm h}^{-1}$ .

#### 4 Conclusions

Herein, we assess the threat of icing conditions at 10 and 20 m due to freezing sea-spray and at the hub height due to precipitation and in-cloud icing. The simulation study encompasses the mid-Atlantic Outer Continental Shelf based on a 21-year WRF dataset from 01 January 2000 to 31 December 2020 and another WRF dataset using year-long simulations from 01 September 2019 to 31 August 2020. In each case, we focus on the wintertime period from November through March. We consider the present icing risk from simulations with no wind farms (NOW-23, NWF) and assess the post-construction adjustments by incorporating the effects of turbines (WFP) in a full buildout of the wind plant lease areas.

396

397 Using an FSS predictability equation (PR), we detect seven events flagged for FSS conditions in NWF with a  
398 total duration of 253 hours during the November 2019 to March 2020 period. All times during the period with  
399 nonzero icing predictability (PR) contain light ice accumulation of less than  $0.7 \text{ cm h}^{-1}$ , which is typical of the mid-  
400 Atlantic bight as assessed from 2000 to 2020. Centered at the RIMA block of lease areas, all seven events have an  
401 associated CAO during the 2019–2020 winter. In the NOW-23 dataset from November 2019 to March 2020, eight  
402 total events are flagged, and all eight correspond with CAO. Over the 21-year climatology, every CAO event has a  
403 corresponding FSS event, although not all FSS events have attendant CAO. Thus, offshore icing conditions may be  
404 forecast with reasonable fidelity through accompanying CAO, although other drivers exist. There is strong  
405 teleconnection between anomalous arctic sea level pressure sea level pressure and CAO, as 93 % of CAO events in  
406 the eastern U.S. contained an antecedent positive arctic sea level pressure anomaly a week in advance (Vavrus et al.,  
407 2006).

408

409 The number of FSS hours exhibit spatial variability, as assessed using our detection criteria of low air sea  
410 surface temperatures and strong winds . The hazards intensify toward higher latitudes where air and sea  
411 temperatures are colder and wind speeds are faster, near the land surface where cold air advects offshore, and by  
412 Nantucket and the Long Island Sound where SSTs are colder. Icing conditions at the hub height, as assessed by low  
413 air temperatures and precipitation or saturated air, are more frequent. The icing hazard is greatest during January  
414 when wind speeds are fast and temperatures are cold. At 10 m in January, favorable conditions for icing occur up to  
415 67 hours. At 20 m in January, the duration of icing conditions is similar at 68 hours. Finally, at the hub height, icing  
416 conditions occur for up to 119 hours east of Cape Cod. Overall, the 2019–2020 winter period is the mildest winter  
417 when considering the 21-year climatology. Although the 2019–2020 winter season has the fewest number of  
418 freezing sea spray hours, all winters contain light ice accumulation rates of  $0.7 \text{ cm h}^{-1}$ .

419

420 The introduction of large wind plants makes a small impact on the icing risk within the wind plant clusters. In  
421 wintertime unstable conditions, which occur 64 % of the time from November 2019 through March 2020, wind  
422 turbines introduce a mean near-surface cooling effect. Despite the enhanced freezing risk from supplementary  
423 cooling, slower wind speeds in the wake mitigate the icing hazard. A mean reduction in wind speeds within wakes  
424 reaches up to  $-0.57 \text{ m s}^{-1}$  in unstable stratification with a mean introduction of cooler air up to  $-0.041 \text{ K}$ . As  
425 assessed using wind speed, air temperature, and SST criteria, the change in FSS risk over the 2019–2020 wintertime  
426 period is a net reduction, by only 15 hours at both 10 and 20 m. The alleviation by slower wind speeds is largest  
427 within the RIMA block of wind plants which contains the greatest number of turbines and the greatest number of  
428 FSS hours relative to other wind energy areas. When assessed using PR centered on the RIMA block, the number of  
429 icing hours increases by 3 with no change to CAO hours. Although the 2019 through 2020 winter period is the  
430 mildest winter, and thus not representative of the 21-year climatology of FSS conditions, this period captures well  
431 the post-construction effects of wind plants. We note that such effects may be more significant during during harsher  
432 winters.

433  
434  
435  
436  
437  
438  
439  
440  
441  
442  
443  
444  
445  
446  
447  
448  
449  
450  
451  
452  
453  
454  
455  
456  
457  
458  
459  
460  
461  
462  
463  
464  
465  
466  
467  
468  
469  
470

Future OCS winter storm frequency may differ due to climate change. For instance, warming Arctic temperatures, which reduce the meridional geopotential height gradient between the Arctic and midlatitudes, can weaken the jet stream. Slower zonal winds and more pronounced Rossby waves amplify the transport of extreme winter weather to the midlatitudes (Cohen et al., 2020). Future East Coast storm activity and temperature may experience modulations based on large-scale teleconnections such as El Niño and the North Atlantic Oscillation (Hall and Booth, 2017). Further, Arctic amplification may increase the strength of teleconnection found between positive Arctic sea level pressure anomalies and CAO (Vavrus et al., 2006).

Finally, we assume that sea spray provides a consistent moisture flux at 10 and 20 m during fast wind conditions, that the droplet size of spray is homogeneous, and that the number distribution by height is constant. The impingement of waves onto offshore structures provides a larger source of moisture than wind-generated spray that is dependent on the wave height and wave period. Future studies may benefit from coupling WRF with wave models, such as Wave Watch III (Tolman et al., 2019) and Simulating WAVes Nearshore (SWAN Team, 2020) for precise modeling of wave characteristics and current dynamics, such as stratified cold pooling around Cape Cod. New satellite methods are being developed to quantify occurrences of freezing sea spray (Line et al., 2022), and future developments could compare the FSS criteria to satellite observations of FSS.

## 5 Code and data availability

The dataset and files that support this work are publicly available. The ERA5 initial and boundary conditions can be downloaded from the ECMWF Climate Data Store at <https://cds.climate.copernicus.eu/cdsapp#!/dataset/reanalysis-era5-pressure-levels?tab=form>. Shapefiles including the bounds for wind energy lease areas are at <https://www.boem.gov/renewable-energy/mapping-and-data/renewable-energy-gis-data>. Wind turbine coordinates and their power and thrust curves are provided at <https://zenodo.org/record/7374283#.Y4YZxC-B1KM>. WRF namelists for NWF and WFP simulations may be acquired from <https://zenodo.org/record/7374239#.Y4YaOy-B1KM>. The NOW-23 simulation output data are available in HDF5 format at <https://doi.org/10.25984/1821404>.

## 6 Author contributions

Conceptualization: JKL. Resources: MO, NB. Methodology: DR, JKL. Software: DR. Formal analysis and visualization: DR. Investigation: DR and JKL. Writing – original draft: DR and JKL. Writing – review and editing: all co-authors. Supervision: JKL.

## 7 Competing interests

At least one of the (co-)authors is a member of the editorial board of Wind Energy Science. Furthermore, Mike Optis co-authored the submitted manuscript while an employee of the National Renewable Energy Laboratory. He has since founded Veer Renewables, which recently released a wind modeling product, WakeMap, which is based on a similar numerical weather prediction modeling framework as the one described in this manuscript. Data from WakeMap is sold to wind energy stakeholders for profit. Public content on WakeMap include a website (htt



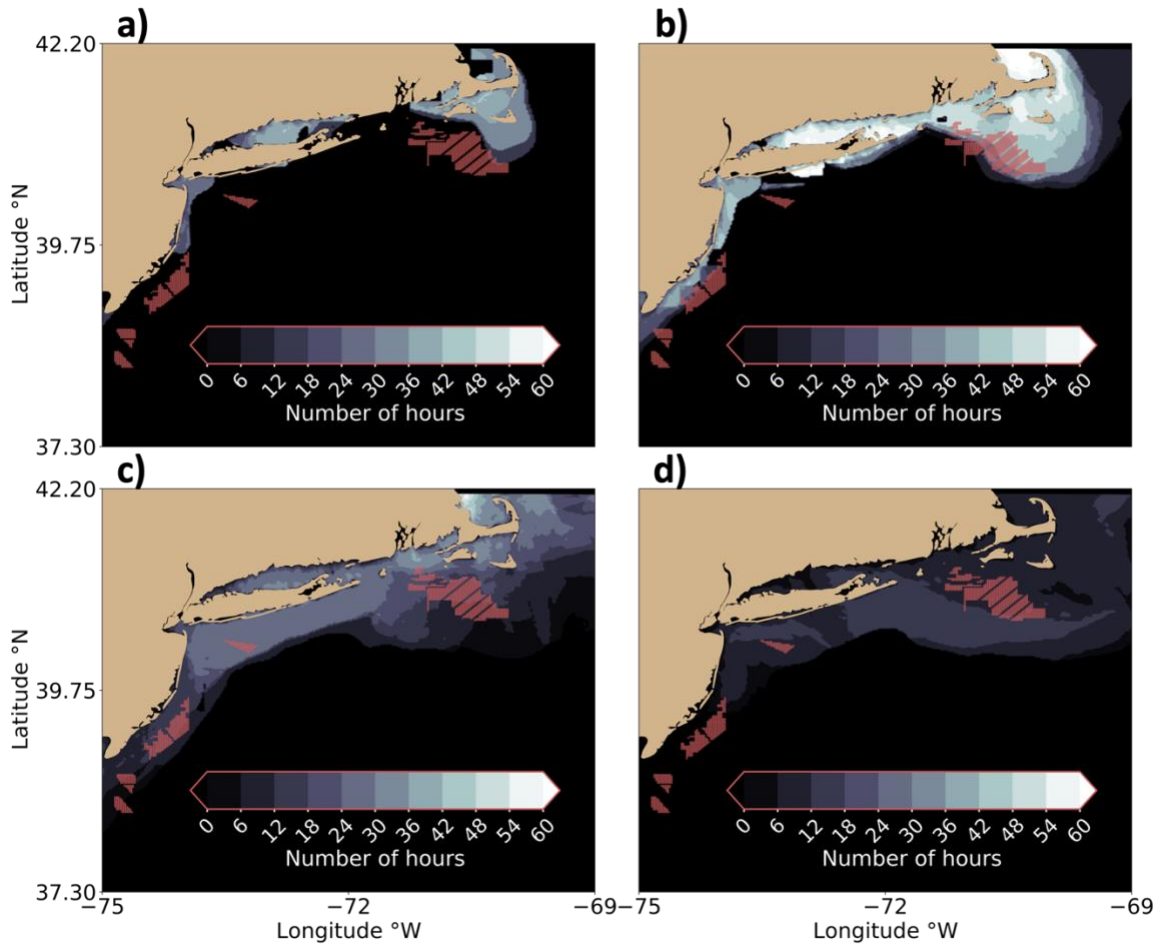
471 J.Mps://veer.eco/wakemap/), a white paper ([https://veer.eco/wp-](https://veer.eco/wp-content/uploads/2023/02/WakeMap_White_Paper_Veer_Renewables.pdf)  
472 [content/uploads/2023/02/WakeMap\\_White\\_Paper\\_Veer\\_Renewables.pdf](https://veer.eco/wp-content/uploads/2023/02/WakeMap_White_Paper_Veer_Renewables.pdf)) and several LinkedIn posts promoting  
473 WakeMap. Mike Optis is the founder and president of Veer Renewables, a for-profit consulting company. Mike  
474 Optis is a shareholder of Veer Renewables and owns 92 % of its stock.

475  
476 **8 Acknowledgements**

477 This work utilized the Alpine high-performance computing resource at the University of Colorado Boulder. Alpine  
478 is jointly funded by the University of Colorado Boulder, the University of Colorado Anschutz, and Colorado State  
479 University. Data storage supported by the University of Colorado Boulder ‘PetaLibrary’ A portion of this research  
480 was performed using computational resources sponsored by the DOE’s Office of Energy Efficiency and Renewable  
481 Energy and located at NREL. This work was authored in part by the National Renewable Energy Laboratory,  
482 operated by Alliance for Sustainable Energy, LLC, for the US Department of Energy (DOE) under contract no. DE-  
483 AC36-08GO28308. Funding was provided by the US Department of Energy Office of Energy Efficiency and  
484 Renewable Energy Wind Energy Technologies Office. Support for the work was also provided by the National  
485 Offshore Wind Research and Development Consortium under agreement no. CRD-19-16351. The views expressed  
486 in the article do not necessarily represent the views of the DOE or the US Government. The US Government retains  
487 and the publisher, by accepting the article for publication, acknowledges that the US Government retains a  
488 nonexclusive, paid-up, irrevocable, worldwide license to publish or reproduce the published form of this work, or  
489 allow others to do so, for US Government purposes.

490 The authors wish to thank Louis Bowers and Sarah McElman for their questions that led to this line of inquiry.

491  
492 **9 Appendices**  
493 **Appendix A**



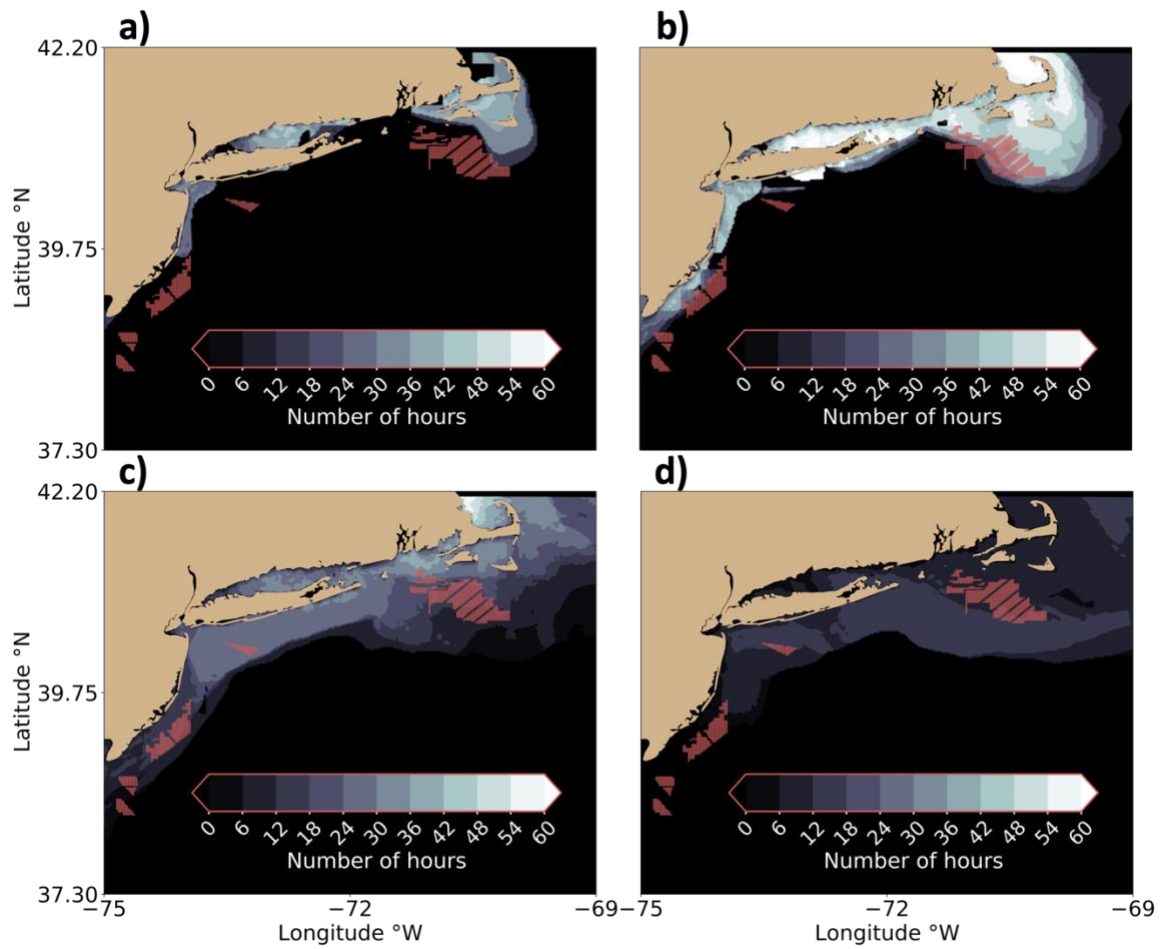
494

495

496

497

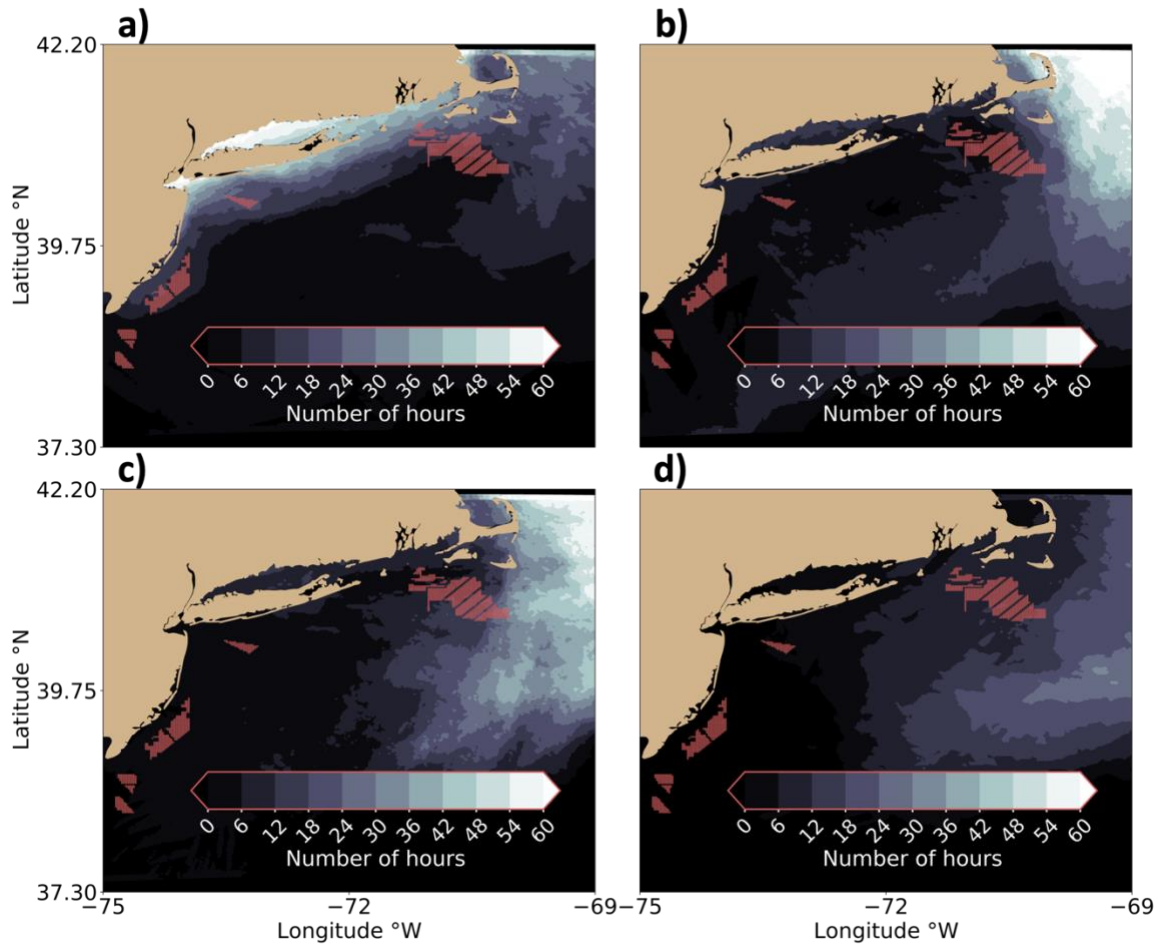
**Figure. A1. The number of freezing hours at 10 m during (a) December 2019, (b) January 2020, (c) February 2020, and (d) March 2020. Lighter contouring indicates higher percentages. Red dots indicate turbine locations.**



498

499 **Figure A2. The number of freezing hours at 20 m during (a) December 2019, (b) January 2020, (c) February 2020, and (d)**  
 500 **March 2020. Lighter contouring indicates higher percentages. Red dots indicate turbine locations.**

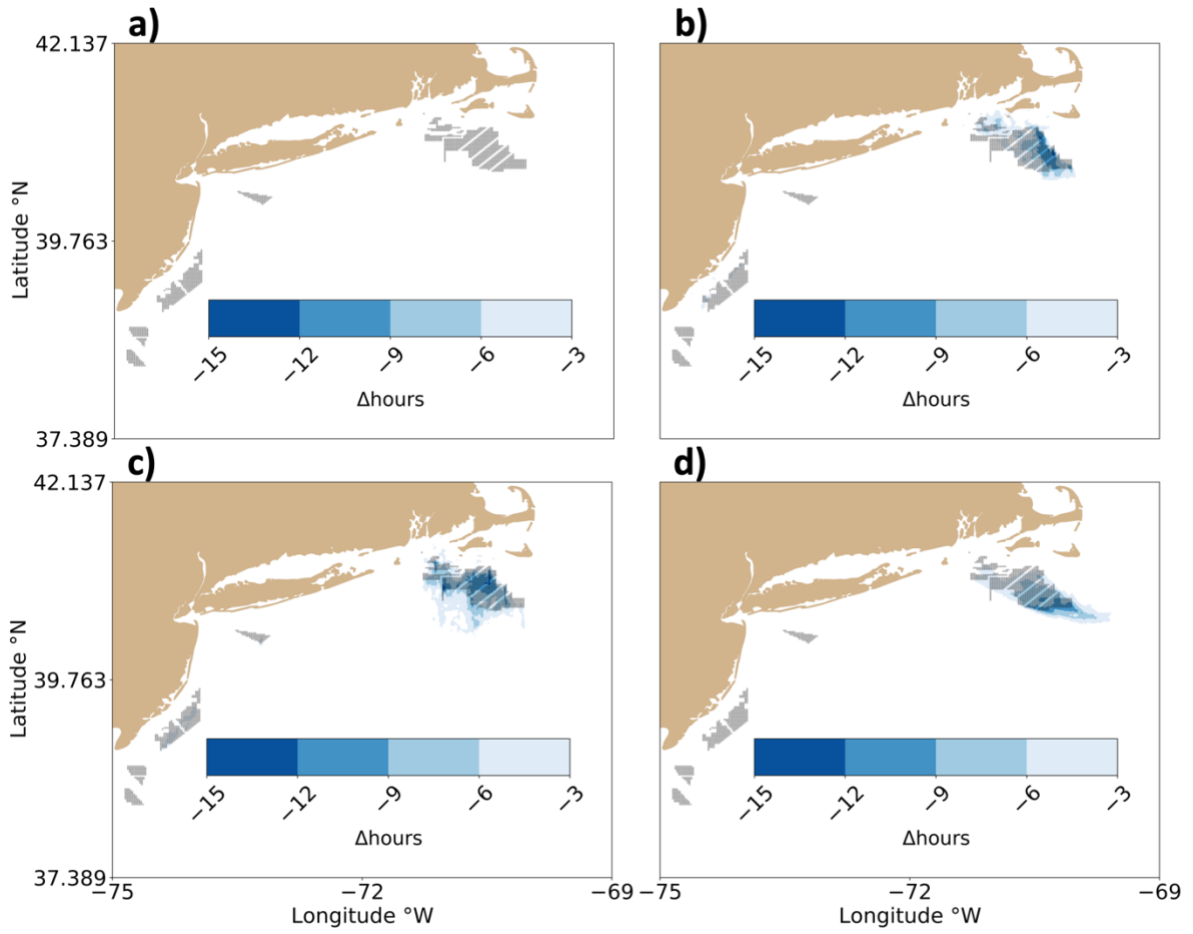
501



502

503 **Figure A3. The number of freezing hours at hub height during (a) December 2019, (b) January 2020, (c) February 2020,**  
 504 **and (d) March 2020. Lighter contouring indicates higher percentages. Note the color scheme is different from**  
 505 **Supplementary Figs. 1 and 2. Red dots indicate turbine locations.**

506



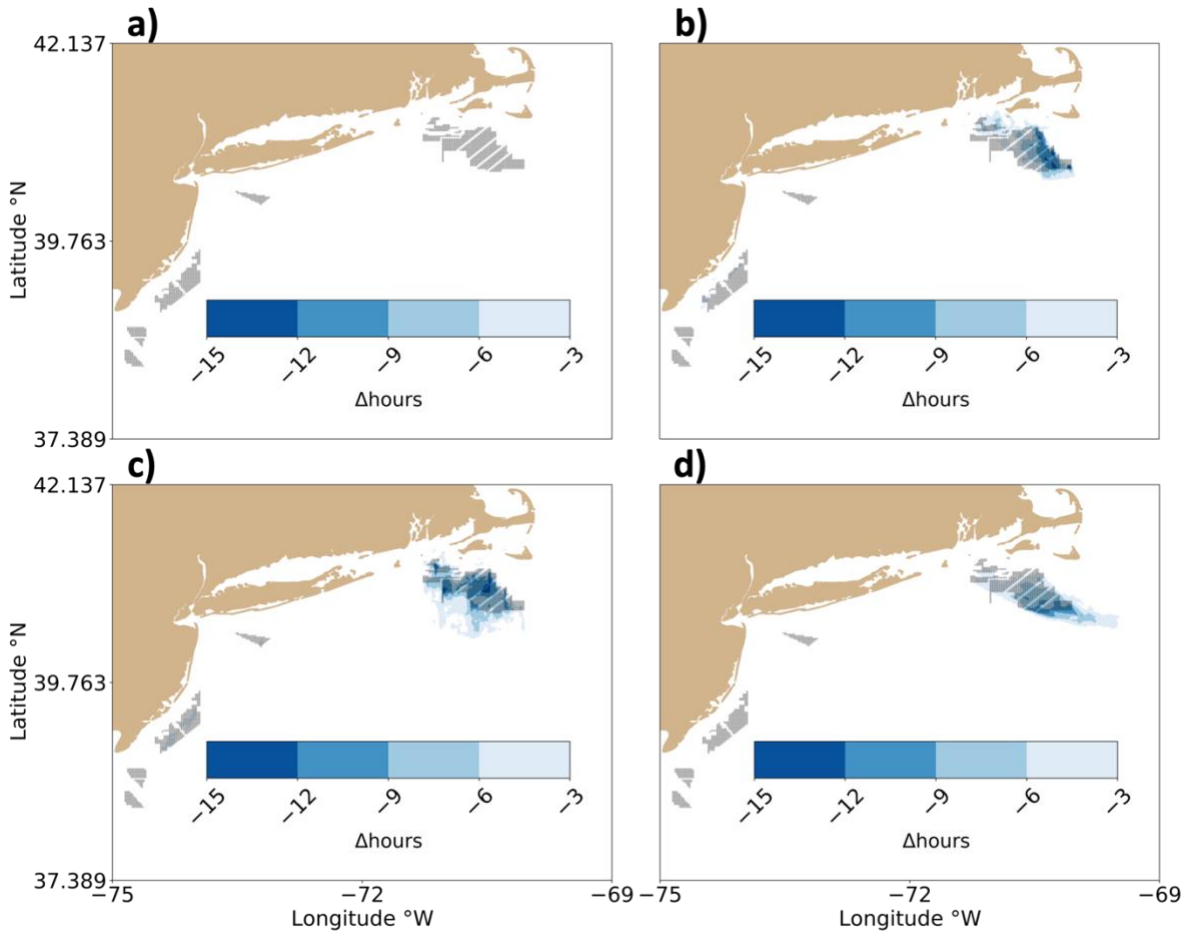
507

508

509

510

**Figure A4.** The (WFP-NWF) difference in freezing hours at 10 m during (a) December 2019, (b) January 2020, (c) February 2020, and (d) March 2020. Blue contouring indicates fewer hours. Gray dots indicate turbine locations.



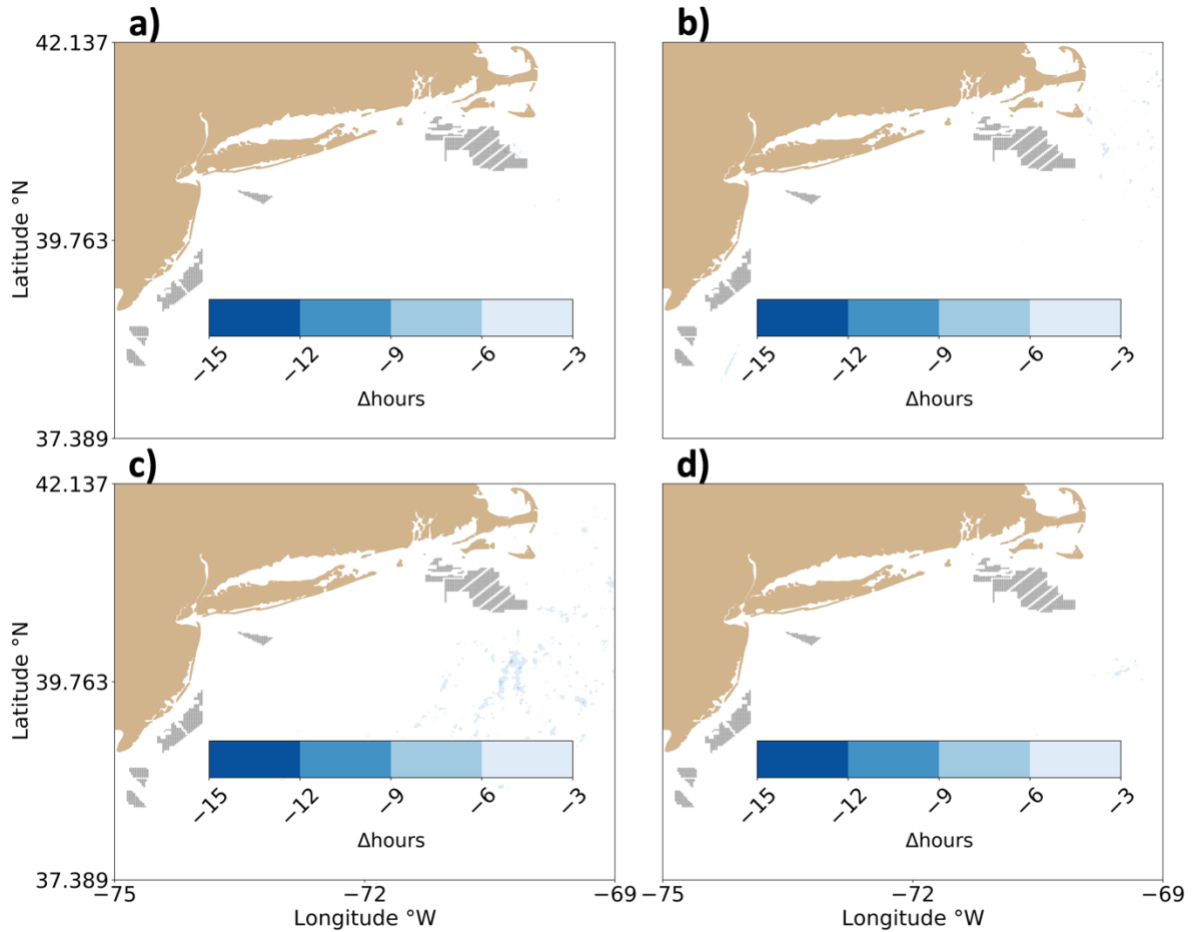
511

512

513

**Figure A5. The (WFP\_0-NWF) difference in freezing hours at 20 m during (a) December 2019, (b) January 2020, (c) February 2020, and (d) March 2020. Blue contouring indicates fewer hours. Gray dots indicate turbine locations.**

514



515  
 516 **Figure A6.** The (WFP-NWF) difference in freezing hours at the hub height during (a) December 2019, (b) January 2020,  
 517 (c) February 2020, and (d) March 2020. Blue contouring indicates fewer hours. Gray dots indicate turbine locations.

518  
 519 **Appendix B**

520 As discussed in Section 2.3, we detect FSS conditions using common thresholds for the meteorological  
 521 conditions (Guest and Luke, 2005; Dehghani-Sanij et al., 2017; Line et al., 2022). These criteria require strong wind  
 522 speeds greater than  $9 \text{ m s}^{-1}$ , cold air temperatures below  $-1.7^\circ \text{ C}$ , and cold SSTs less than  $7^\circ \text{ C}$ . As reviewed by  
 523 Dehghani-Sanij et al., (2017), FSS conditions are promising when the air temperature is below either  $-1.7^\circ \text{ C}$  or  $-2^\circ$   
 524  $\text{C}$  to account for the lower freezing point of saline ocean water; the salt content of which determines this threshold.  
 525 Although SST thresholds of  $5^\circ \text{ C}$  or  $7^\circ \text{ C}$  are prevalent, a threshold up to  $8.9^\circ \text{ C}$  has been used (U.S. Navy, 1988).  
 526 As such, we quantify some of the uncertainty by calculating the number of hours that FSS conditions occur using  
 527 conservative thresholds, which produce fewer icing hours (FEWER), and liberal thresholds, which promote more  
 528 icing hours (MORE) (Table B1). As there is wider agreement regarding the wind speed threshold (Dehghani-Sanij et  
 529 al., 2017; Guest and Luke, 2005; Line et al., 2022; Ross and Cardone, 1974; Monahan et al., 1983; Monahan and  
 530 MacNiocaill, 1986), we hold it constant. Due to computational constraints, we only assess the number of icing hours  
 531 throughout the domain at 10 m and during January 2020 because it has the greatest number of icing hours.  
 532

533

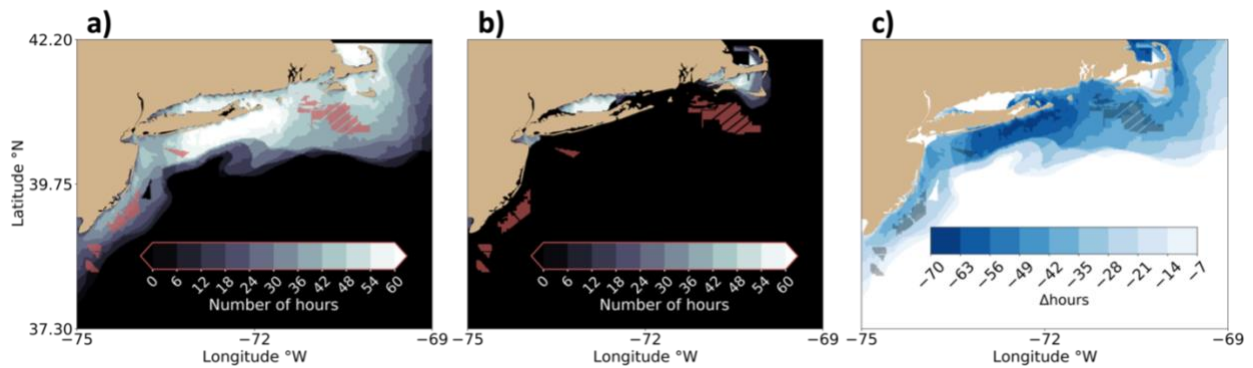
**Table B1. Icing detection criteria by sensitivity analysis type.**

Acronym	Air temperature	Sea surface temperature	Wind speed
FEWER	<-2° C	<5° C	>9 m s <sup>-1</sup>
MORE	<-1.7° C	<8.9° C	>9 m s <sup>-1</sup>

534

535 As expected, more conservative thresholds produce fewer FSS hours and vice versa (Fig. B1a,b,c). In  
 536 FEWER, the meteorological conditions conducive to icing maximize at 60 hours. Using more liberal criteria in  
 537 MORE, the maximum number of hours increases to 67. Despite the small change in the maximum number of hours  
 538 FSS occurs, the regional variation is large; the area covered by icing conditions increases from 8,924 km<sup>2</sup> to 135,244  
 539 km<sup>2</sup> from FEWER to MORE, or roughly 15 times greater than FEWER, or 2.2 times greater than our production set  
 540 of criteria. Regional variability follows SST patterns and only occurs in FEWER where the SST is relatively cold in  
 541 the Long Island Sound and Nantucket Sound (Table B1b), as discussed previously.

542

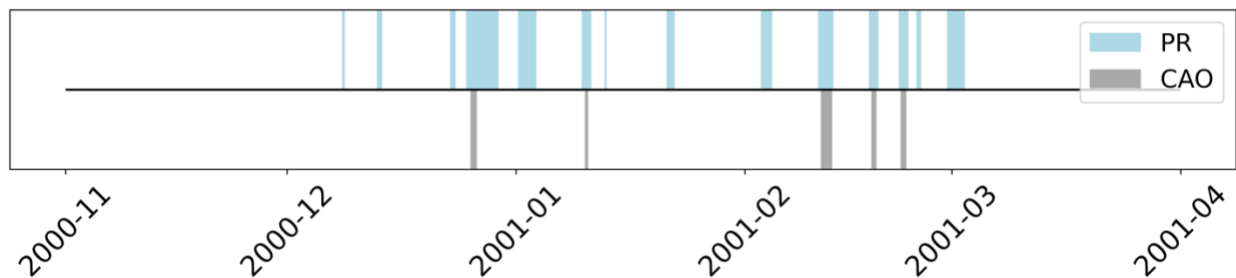


543

544 **Fig. B1. The number of hours FSS conditions occur during January 2020 at 10 m in NWF using thresholds for (a)**  
 545 **FEWER, (b) MORE, and (c) the (FEWER-MORE) difference. Lighter contouring indicates more freezing hours in (a)**  
 546 **and (b). Darker blues represent a larger reduction in number of hours in (c). Turbine locations are shown as red dots in**  
 547 **(a) and (b) and as black dots in (c).**

548

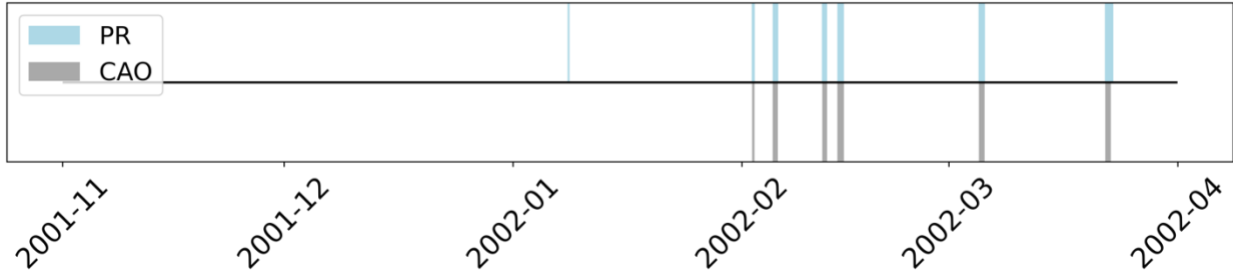
549 **Appendix C**



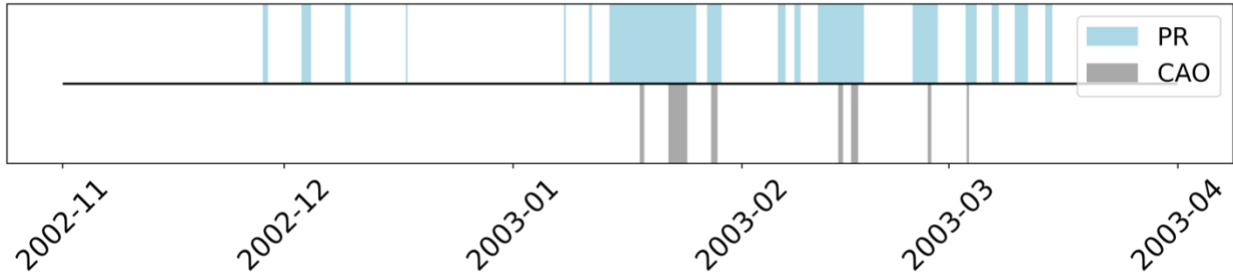
550

551 **Fig. C1. Time series of CAO and FSS events from November 2000 to April 2001. Light-blue shading indicates the**  
 552 **duration of nonzero PR and gray shading indicates the duration of detected CAO from NOW-23.**

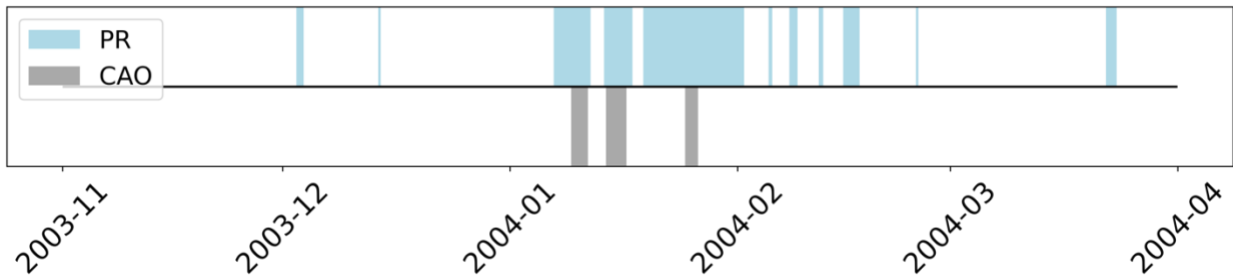




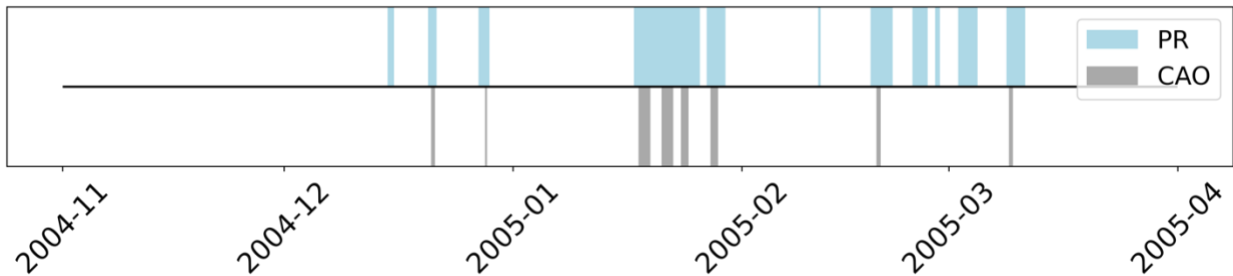
553  
554 Fig. C2. Time series of CAO and FSS events from November 2001 to April 2002. Light-blue shading indicates the  
555 duration of nonzero PR and gray shading indicates the duration of detected CAO from NOW-23.



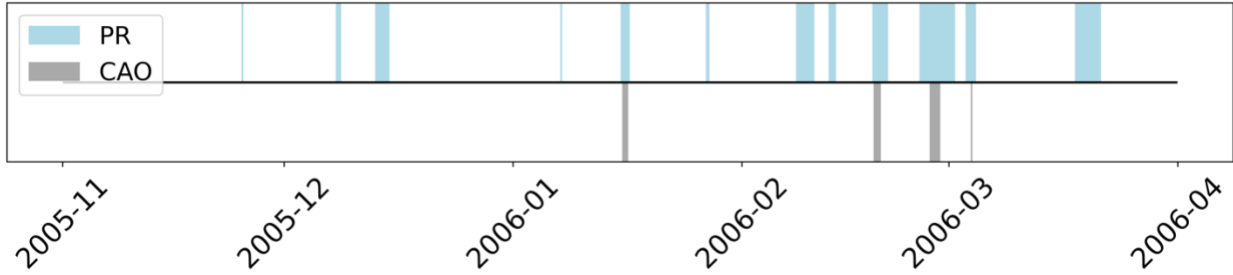
556  
557 Fig. C3. Time series of CAO and FSS events from November 2002 to April 2003. Light-blue shading indicates the  
558 duration of nonzero PR and gray shading indicates the duration of detected CAO from NOW-23.



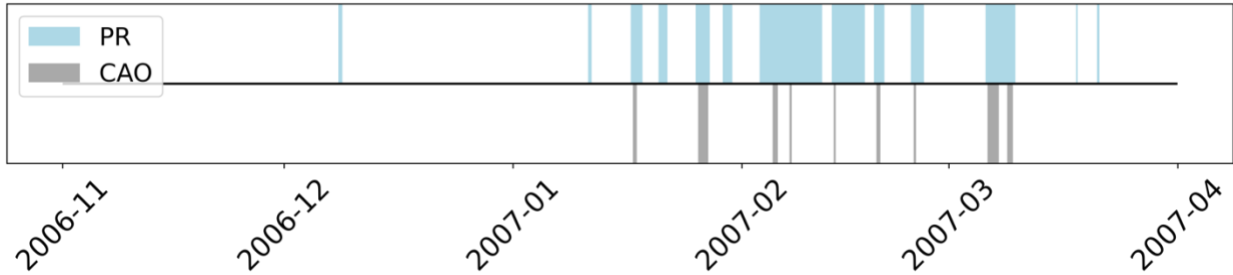
559  
560 Fig. C4. Time series of CAO and FSS events from November 2003 to April 2004. Light-blue shading indicates the  
561 duration of nonzero PR and gray shading indicates the duration of detected CAO from NOW-23.



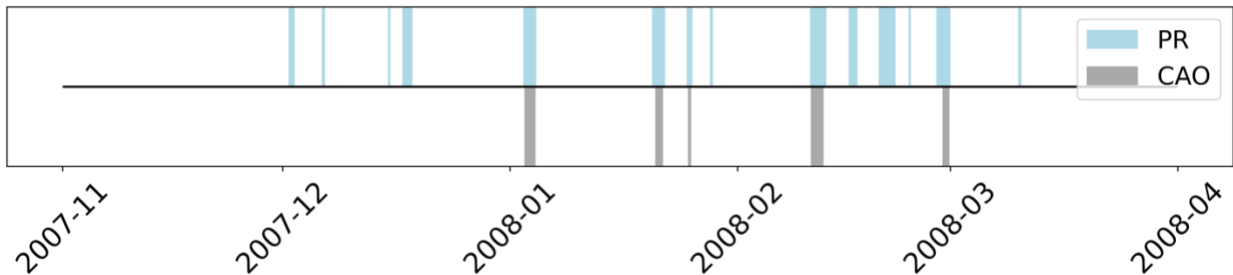
562  
563 Fig. C5. Time series of CAO and FSS events from November 2004 to April 2005. Light-blue shading indicates the  
564 duration of nonzero PR and gray shading indicates the duration of detected CAO from NOW-23.



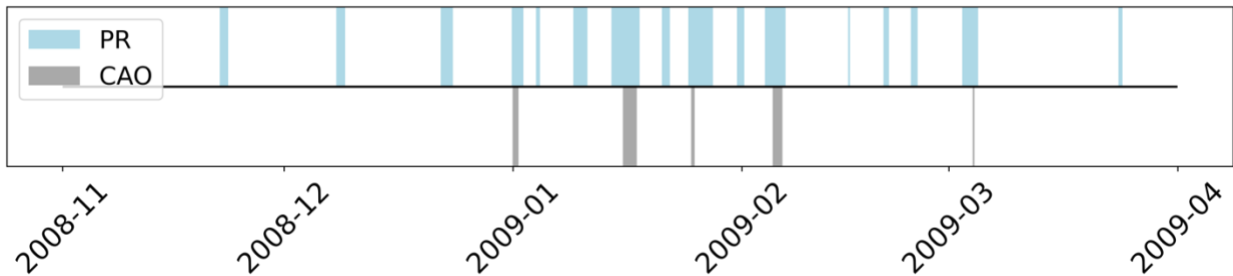
565  
566 **Fig. C6. Time series of CAO and FSS events from November 2005 to April 2006. Light-blue shading indicates the**  
567 **duration of nonzero PR and gray shading indicates the duration of detected CAO from NOW-23.**



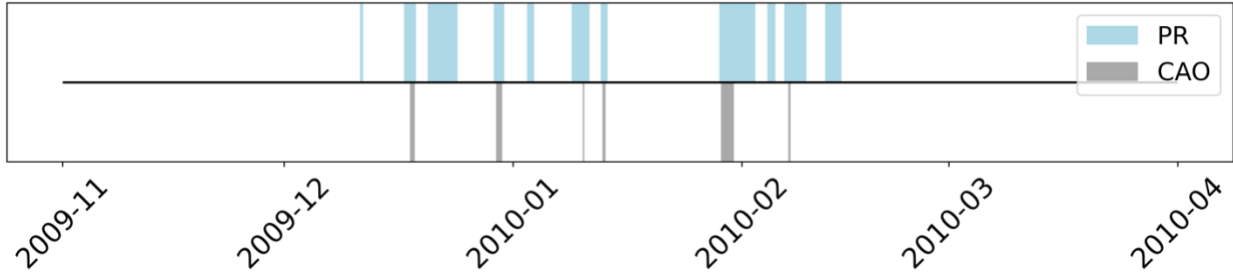
568  
569 **Fig. C7. Time series of CAO and FSS events from November 2006 to April 2007. Light-blue shading indicates the**  
570 **duration of nonzero PR and gray shading indicates the duration of detected CAO from NOW-23.**



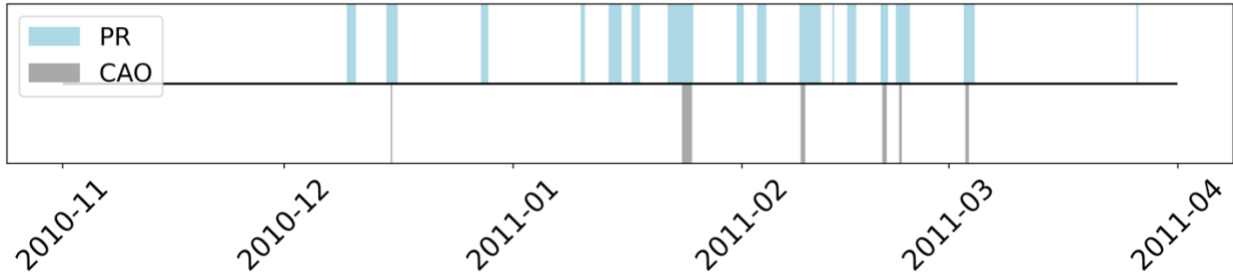
571  
572 **Fig. C8. Time series of CAO and FSS events from November 2007 to April 2008. Light-blue shading indicates the**  
573 **duration of nonzero PR and gray shading indicates the duration of detected CAO from NOW-23.**



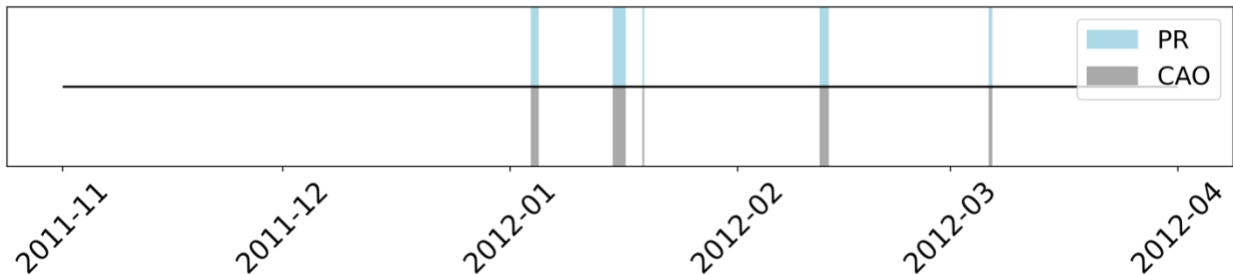
574  
575 **Fig. C9. Time series of CAO and FSS events from November 2008 to April 2009. Light-blue shading indicates the**  
576 **duration of nonzero PR and gray shading indicates the duration of detected CAO from NOW-23.**



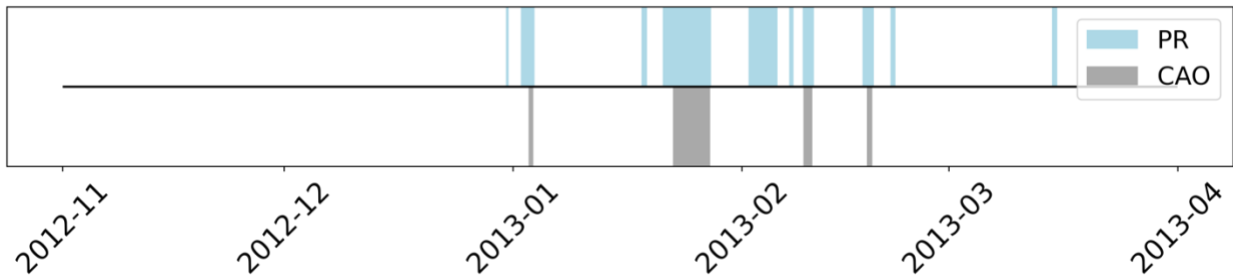
577  
578 **Fig. C10.** Time series of CAO and FSS events from November 2009 to April 2010. Light-blue shading indicates the  
579 duration of nonzero PR and gray shading indicates the duration of detected CAO from NOW-23.



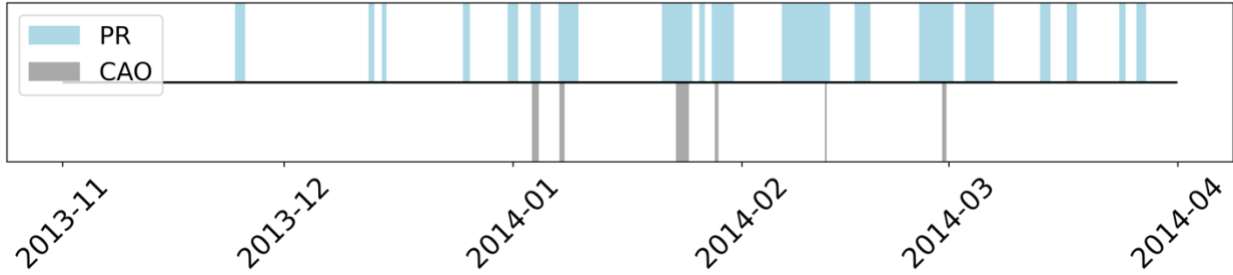
580  
581 **Fig. C11.** Time series of CAO and FSS events from November 2010 to April 2011. Light-blue shading indicates the  
582 duration of nonzero PR and gray shading indicates the duration of detected CAO from NOW-23.



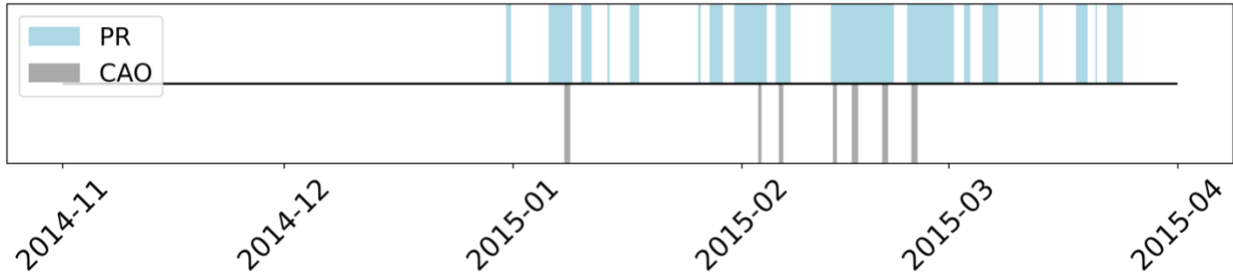
583  
584 **Fig. C12.** Time series of CAO and FSS events from November 2011 to April 2012. Light-blue shading indicates the  
585 duration of nonzero PR and gray shading indicates the duration of detected CAO from NOW-23.



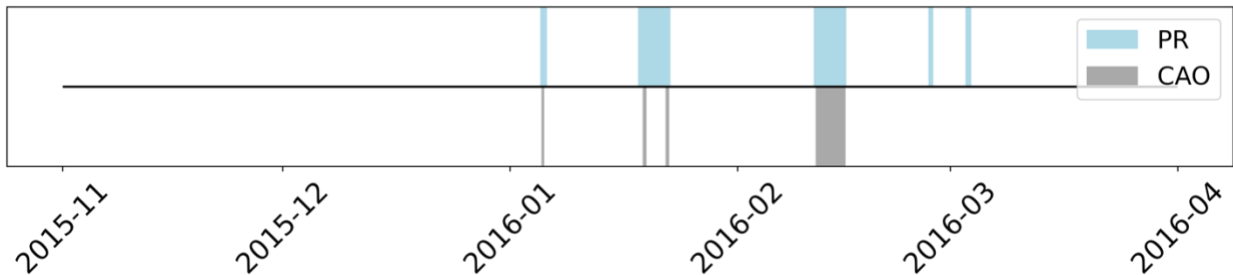
586  
587 **Fig. C13.** Time series of CAO and FSS events from November 2012 to April 2013. Light-blue shading indicates the  
588 duration of nonzero PR and gray shading indicates the duration of detected CAO from NOW-23.



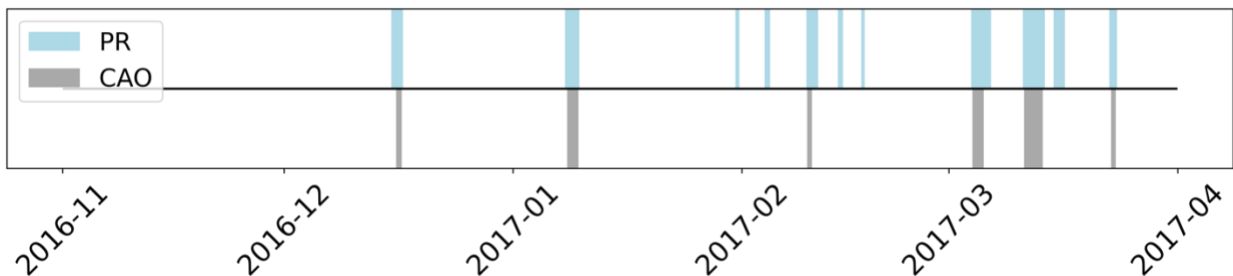
589  
590 **Fig. C14. Time series of CAO and FSS events from November 2013 to April 2014. Light-blue shading indicates the**  
591 **duration of nonzero PR and gray shading indicates the duration of detected CAO from NOW-23.**



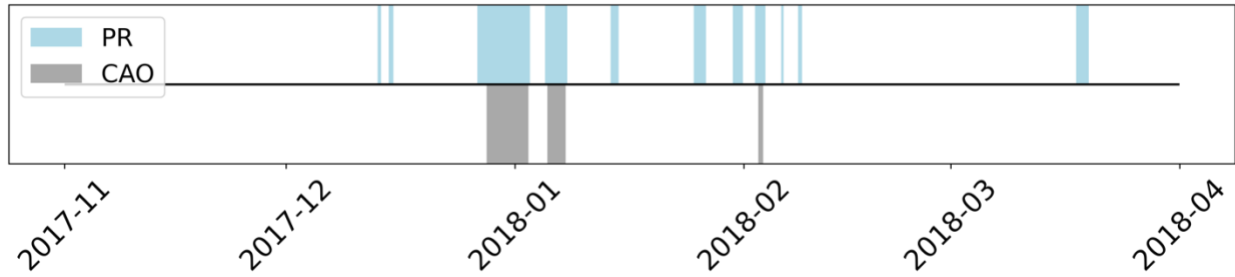
592  
593 **Fig. C15. Time series of CAO and FSS events from November 2014 to April 2015. Light-blue shading indicates the**  
594 **duration of nonzero PR and gray shading indicates the duration of detected CAO from NOW-23.**



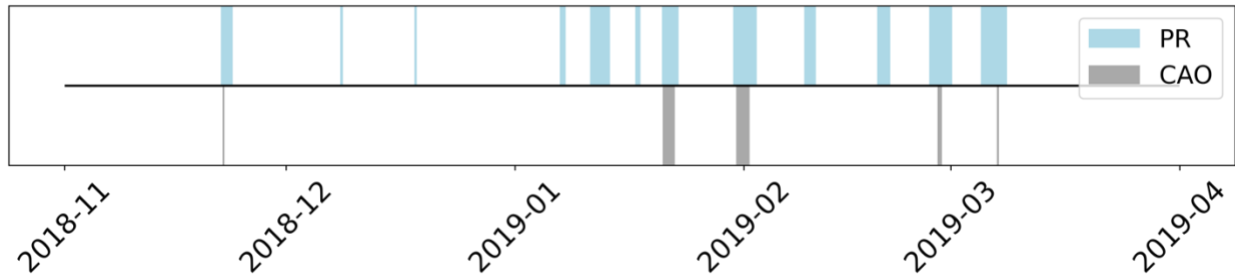
595  
596 **Fig. C16. Time series of CAO and FSS events from November 2015 to April 2016. Light-blue shading indicates the**  
597 **duration of nonzero PR and gray shading indicates the duration of detected CAO from NOW-23.**



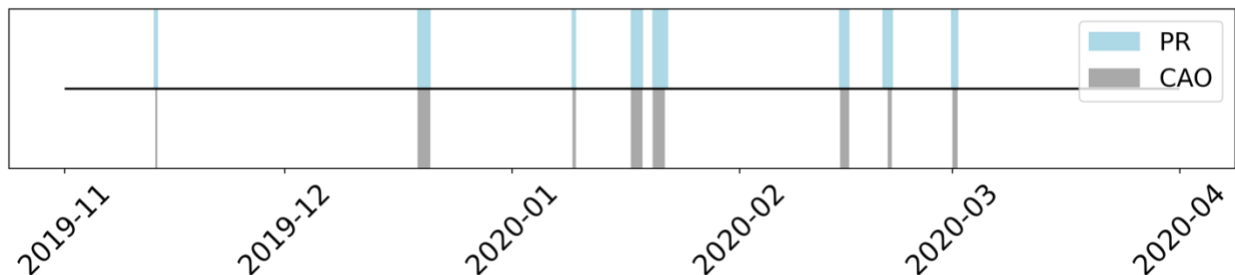
598  
599 **Fig. C17. Time series of CAO and FSS events from November 2016 to April 2017. Light-blue shading indicates the**  
600 **duration of nonzero PR and gray shading indicates the duration of detected CAO from NOW-23.**



601  
602 **Fig. C18. Time series of CAO and FSS events from November 2017 to April 2018. Light-blue shading indicates the**  
603 **duration of nonzero PR and gray shading indicates the duration of detected CAO from NOW-23.**



604  
605 **Fig. C19. Time series of CAO and FSS events from November 2018 to April 2019. Light-blue shading indicates the**  
606 **duration of nonzero PR and gray shading indicates the duration of detected CAO from NOW-23.**



607  
608 **Fig. C20. Time series of CAO and FSS events from November 2019 to April 2020. Light-blue shading indicates the**  
609 **duration of nonzero PR and gray shading indicates the duration of detected CAO from NOW-23.**

610  
611 **10 References**

612  
613 Alexander, M. and Scott, J.: The influence of ENSO on air-sea interaction in the Atlantic, *Geophysical Research*  
614 *Letters*, 29, 46-1-46-4, <https://doi.org/10.1029/2001GL014347>, 2002.

615 Archer, C. L., Colle, B. A., Veron, D. L., Veron, F., and Sienkiewicz, M. J.: On the predominance of unstable  
616 atmospheric conditions in the marine boundary layer offshore of the U.S. northeastern coast, *Journal of Geophysical*  
617 *Research: Atmospheres*, 121, 8869–8885, <https://doi.org/10.1002/2016JD024896>, 2016.

618 Archer, C. L., Wu, S., Ma, Y., and Jiménez, P. A.: Two Corrections for Turbulent Kinetic Energy Generated by  
619 Wind Farms in the WRF Model, *Monthly Weather Review*, 148, 4823–4835, [https://doi.org/10.1175/MWR-D-20-](https://doi.org/10.1175/MWR-D-20-0097.1)  
620 [0097.1](https://doi.org/10.1175/MWR-D-20-0097.1), 2020.

621 Atkinson, B. W. and Wu Zhang, J.: Mesoscale shallow convection in the atmosphere, *Reviews of Geophysics*, 34,  
622 403–431, <https://doi.org/10.1029/96RG02623>, 1996.

623 Battisti, L., Fedrizzi, R., Brighenti, A., and Laakso, T.: Sea ice and icing risk for offshore wind turbines,  
624 *Proceedings of the OWEMES*, 20–22,

625 <https://citeseerx.ist.psu.edu/document?repid=rep1&type=pdf&doi=8bb110a8c86abf785b1b019dcc37150f09de90ae>,  
626 2006.

627 Beiter, P., Musial, W., Duffy, P., Cooperman, A., Shields, M., Heimiller, D., and Optis, M.: The Cost of Floating  
628 Offshore Wind Energy in California Between 2019 and 2032, NREL/TP-5000-77384,  
629 <https://doi.org/10.2172/1710181>, 2020.

630 Bodini, N., Lundquist, J. K., and Kirincich, A.: U.S. East Coast Lidar Measurements Show Offshore Wind Turbines  
631 Will Encounter Very Low Atmospheric Turbulence, *Geophysical Research Letters*, 46, 5582–5591,  
632 <https://doi.org/10.1029/2019GL082636>, 2019.

633 Bodini, N., Optis, M., Redfern, S., Rosencrans, D., Rybchuk, A., Lundquist, J. K., Pronk, V., Castagneri, S.,  
634 Purkayastha, A., Draxl, C., Krishnamurthy, R., Young, E., Roberts, B., Rosenlieb, E., and Musial, W.: The 2023  
635 National Offshore Wind data set (NOW-23), *Earth System Science Data*, 16, 1965–2006,  
636 <https://doi.org/10.5194/essd-16-1965-2024>, 2024.

637 Chapman, D. C., Barth, J. A., Beardsley, R. C., and Fairbanks, R. G.: On the Continuity of Mean Flow between the  
638 Scotian Shelf and the Middle Atlantic Bight, *Journal of Physical Oceanography*, 16, 758–772,  
639 [https://doi.org/10.1175/1520-0485\(1986\)016<0758:OTCOMF>2.0.CO;2](https://doi.org/10.1175/1520-0485(1986)016<0758:OTCOMF>2.0.CO;2), 1986.

640 Cohen, J., Zhang, X., Francis, J., Jung, T., Kwok, R., Overland, J., Ballinger, T. J., Bhatt, U. S., Chen, H. W.,  
641 Coumou, D., Feldstein, S., Gu, H., Handorf, D., Henderson, G., Ionita, M., Kretschmer, M., Laliberte, F., Lee, S.,  
642 Linderholm, H. W., Maslowski, W., Peings, Y., Pfeiffer, K., Rigor, I., Semmler, T., Stroeve, J., Taylor, P. C.,  
643 Vavrus, S., Vihma, T., Wang, S., Wendisch, M., Wu, Y., and Yoon, J.: Divergent consensus on Arctic  
644 amplification influence on midlatitude severe winter weather, *Nat. Clim. Chang.*, 10, 20–29,  
645 <https://doi.org/10.1038/s41558-019-0662-y>, 2020.

646 Contreras Montoya, L. T., Lain, S., and Ilinca, A.: A Review on the Estimation of Power Loss Due to Icing in Wind  
647 Turbines, *Energies*, 15, 1083, <https://doi.org/10.3390/en15031083>, 2022.

648 Dehghani-Sanij, A. R., Dehghani, S. R., Naterer, G. F., and Muzychka, Y. S.: Sea spray icing phenomena on marine  
649 vessels and offshore structures: Review and formulation, *Ocean Engineering*, 132, 25–39,  
650 <https://doi.org/10.1016/j.oceaneng.2017.01.016>, 2017.

651 Donlon, C. J., Martin, M., Stark, J., Roberts-Jones, J., Fiedler, E., and Wimmer, W.: The Operational Sea Surface  
652 Temperature and Sea Ice Analysis (OSTIA) system, *Remote Sensing of Environment*, 116, 140–158,  
653 <https://doi.org/10.1016/j.rse.2010.10.017>, 2012.

654 Ferrel, W.: *Nashville Journal of Medicine and Surgery*, 11, 7–19,  
655 <https://empslocal.ex.ac.uk/people/staff/gv219/classics.d/ferrel-nashville56.pdf>, 1856.

656 Ferrier, B. S., Jin, Y., Lin, Y., Black, T., Rogers, E., and DiMego, G.: Implementation of a new grid-scale cloud and  
657 precipitation scheme in the NCEP Eta model, *Amer. Meteor. Soc. Conf. on Weather Analysis and Forecasting*, 19,  
658 [https://scholar.google.com/scholar?hl=en&as\\_sdt=0%2C6&q=Implementation+of+a+new+grid-  
659 scale+cloud+and+precipitation+scheme+in+the+NCEP+Eta+model&btnG=](https://scholar.google.com/scholar?hl=en&as_sdt=0%2C6&q=Implementation+of+a+new+grid-scale+cloud+and+precipitation+scheme+in+the+NCEP+Eta+model&btnG=), 2002.

660 Fitch, A. C., Olson, J. B., Lundquist, J. K., Dudhia, J., Gupta, A. K., Michalakes, J., and Barstad, I.: Local and  
661 Mesoscale Impacts of Wind Farms as Parameterized in a Mesoscale NWP Model, *Monthly Weather Review*, 140,  
662 3017–3038, <https://doi.org/10.1175/MWR-D-11-00352.1>, 2012.

663 Fitch, A. C., Lundquist, J. K., and Olson, J. B.: Mesoscale Influences of Wind Farms throughout a Diurnal Cycle,  
664 *Mon. Wea. Rev.*, 141, 2173–2198, <https://doi.org/10.1175/MWR-D-12-00185.1>, 2013.

665 Gao, L. and Hong, J.: Wind turbine performance in natural icing environments: A field characterization, *Cold  
666 Regions Science and Technology*, 181, 103193, <https://doi.org/10.1016/j.coldregions.2020.103193>, 2021.

667 Gao, L. and Hu, H.: Wind turbine icing characteristics and icing-induced power losses to utility-scale wind turbines,  
668 Proceedings of the National Academy of Sciences, 118, e2111461118, <https://doi.org/10.1073/pnas.2111461118>,  
669 2021.

670 Geerts, B., Giangrande, S. E., McFarquhar, G. M., Xue, L., Abel, S. J., Comstock, J. M., Crewell, S., DeMott, P. J.,  
671 Ebell, K., Field, P., Hill, T. C. J., Hunzinger, A., Jensen, M. P., Johnson, K. L., Juliano, T. W., Kollias, P., Kosovic,  
672 B., Lackner, C., Luke, E., Lüpkes, C., Matthews, A. A., Neggers, R., Ovchinnikov, M., Powers, H., Shupe, M. D.,  
673 Spengler, T., Swanson, B. E., Tjernström, M., Theisen, A. K., Wales, N. A., Wang, Y., Wendisch, M., and Wu, P.:  
674 The COMBLE Campaign: A Study of Marine Boundary Layer Clouds in Arctic Cold-Air Outbreaks, Bulletin of the  
675 American Meteorological Society, 103, E1371–E1389, <https://doi.org/10.1175/BAMS-D-21-0044.1>, 2022.

676 Golbazi, M., Archer, C. L., and Alessandrini, S.: Surface impacts of large offshore wind farms, Environ. Res. Lett.,  
677 17, 064021, <https://doi.org/10.1088/1748-9326/ac6e49>, 2022.

678 Gómez, B. and Miguez-Macho, G.: The impact of wave number selection and spin-up time in spectral nudging,  
679 Quarterly Journal of the Royal Meteorological Society, 143, 1772–1786, <https://doi.org/10.1002/qj.3032>, 2017.

680 Gryning, S.-E., Batchvarova, E., Brümmner, B., Jørgensen, H., and Larsen, S.: On the extension of the wind profile  
681 over homogeneous terrain beyond the surface boundary layer, Boundary-Layer Meteorol, 124, 251–268,  
682 <https://doi.org/10.1007/s10546-007-9166-9>, 2007.

683 Guest, P. and Luke, R.: The Power of Wind and Water, Mariners Weather Log,  
684 [https://www.vos.noaa.gov/MWL/dec\\_05/ves.shtml](https://www.vos.noaa.gov/MWL/dec_05/ves.shtml), 2005.

685 Hall, T. and Booth, J. F.: SynthETC: A Statistical Model for Severe Winter Storm Hazard on Eastern North  
686 America, Journal of Climate, 30, 5329–5343, <https://doi.org/10.1175/JCLI-D-16-0711.1>, 2017.

687 Hersbach, H., Bell, B., Berrisford, P., Hirahara, S., Horányi, A., Muñoz-Sabater, J., Nicolas, J., Peubey, C., Radu,  
688 R., Schepers, D., Simmons, A., Soci, C., Abdalla, S., Abellan, X., Balsamo, G., Bechtold, P., Biavati, G., Bidlot, J.,  
689 Bonavita, M., De Chiara, G., Dahlgren, P., Dee, D., Diamantakis, M., Dragani, R., Flemming, J., Forbes, R.,  
690 Fuentes, M., Geer, A., Haimberger, L., Healy, S., Hogan, R. J., Hólm, E., Janisková, M., Keeley, S., Laloyaux, P.,  
691 Lopez, P., Lupu, C., Radnoti, G., de Rosnay, P., Rozum, I., Vamborg, F., Villaume, S., and Thépaut, J.-N.: The  
692 ERA5 global reanalysis, Quarterly Journal of the Royal Meteorological Society, 146, 1999–2049,  
693 <https://doi.org/10.1002/qj.3803>, 2020.

694 Hirsch, R. M., Slack, J. R., and Smith, R. A.: Techniques of trend analysis for monthly water quality data, Water  
695 Resources Research, <https://doi.org/10.1029/WR018i001p00107>, 1982.

696 Hussain, M. M. and Mahmud, I.: pyMannKendall: a python package for non parametric Mann Kendall family of  
697 trend tests., Journal of Open Source Software, 4, 1556, <https://doi.org/10.21105/joss.01556>, 2019.

698 Iacono, M. J., Delamere, J. S., Mlawer, E. J., Shephard, M. W., Clough, S. A., and Collins, W. D.: Radiative forcing  
699 by long-lived greenhouse gases: Calculations with the AER radiative transfer models, Journal of Geophysical  
700 Research: Atmospheres, 113, <https://doi.org/10.1029/2008JD009944>, 2008.

701 IEA: Available Technologies for Wind Energy in Cold Climates – report, [https://iea-wind.org/wp-](https://iea-wind.org/wp-content/uploads/2021/09/Lehtomaki-et-al.-2018-Available-Technologies-for-Wind-Energy-in-Cold-Climates-report-2-nd-edition-2018.pdf)  
702 [content/uploads/2021/09/Lehtomaki-et-al.-2018-Available-Technologies-for-Wind-Energy-in-Cold-Climates-report-](https://iea-wind.org/wp-content/uploads/2021/09/Lehtomaki-et-al.-2018-Available-Technologies-for-Wind-Energy-in-Cold-Climates-report-2-nd-edition-2018.pdf)  
703 [2-nd-edition-2018.pdf](https://iea-wind.org/wp-content/uploads/2021/09/Lehtomaki-et-al.-2018-Available-Technologies-for-Wind-Energy-in-Cold-Climates-report-2-nd-edition-2018.pdf), 2018.

704 ISO: Atmospheric Icing of Structures, Geneva, Switzerland, ISO-12494:2017,  
705 <https://cdn.standards.iteh.ai/samples/72443/2fb2033c3f844304b66281607516ec58/ISO-12494-2017.pdf>, 2017.

706 Kain, J. S.: The Kain–Fritsch Convective Parameterization: An Update, Journal of Applied Meteorology and  
707 Climatology, 43, 170–181, [https://doi.org/10.1175/1520-0450\(2004\)043<0170:TKCPAU>2.0.CO;2](https://doi.org/10.1175/1520-0450(2004)043<0170:TKCPAU>2.0.CO;2), 2004.

708 Kraegel, L.: Destination likely sank after accumulating ice in heavy freezing spray, report says:  
709 [https://www.ktoo.org/2018/07/16/destination-likely-sank-after-accumulating-ice-in-heavy-freezing-spray-report-](https://www.ktoo.org/2018/07/16/destination-likely-sank-after-accumulating-ice-in-heavy-freezing-spray-report-says/)  
710 [says/](https://www.ktoo.org/2018/07/16/destination-likely-sank-after-accumulating-ice-in-heavy-freezing-spray-report-says/), last access: 12 April 2023.

711 Kraj, A. G. and Bibeau, E. L.: Phases of icing on wind turbine blades characterized by ice accumulation, *Renewable*  
712 *Energy*, 35, 966–972, <https://doi.org/10.1016/j.renene.2009.09.013>, 2010.

713 Line, W. E., Grasso, L., Hillger, D., Dierking, C., Jacobs, A., and Shea, S.: Using NOAA Satellite Imagery to Detect  
714 and Track Hazardous Sea Spray in the High Latitudes, *Weather and Forecasting*, 37, 351–369,  
715 <https://doi.org/10.1175/WAF-D-21-0137.1>, 2022.

716 NTSB: NTSB announces the probable cause of the sunken Scandies Rose:  
717 <https://www.alaskanewssource.com/2021/06/29/ntsb-announce-probable-cause-sunken-scandies-rose/>, last access:  
718 12 April 2023.

719 Madi, E., Pope, K., Huang, W., and Iqbal, T.: A review of integrating ice detection and mitigation for wind turbine  
720 blades, *Renewable and Sustainable Energy Reviews*, 103, 269–281, <https://doi.org/10.1016/j.rser.2018.12.019>,  
721 2019.

722 Martini, F., Contreras Montoya, L. T., and Ilinca, A.: Review of Wind Turbine Icing Modelling Approaches,  
723 *Energies*, 14, 5207, <https://doi.org/10.3390/en14165207>, 2021.

724 Monahan, E. C. and MacNiocaill, G.: *Oceanic Whitecaps And Their Role in Air-Sea Exchange Processes*, D Reidel  
725 Publishing Company, e-ISBN-13: 978-94-009-4668-2, <https://link.springer.com/book/10.1007/978-94-009-4668-2>,  
726 1986.

727 Monahan, E. C., Fairall, C. W., Davidson, K. L., and Boyle, P. J.: Observed inter-relations between 10m winds,  
728 ocean whitecaps and marine aerosols, *Quarterly Journal of the Royal Meteorological Society*, 109, 379–392,  
729 <https://doi.org/10.1002/qj.49710946010>, 1983.

730 Monin, A. S. and Obukhov, A. M.: Basic laws of turbulent mixing in the surface layer of the atmosphere, *Tr. Akad.*  
731 *Nauk SSSR Geophys. Inst.*, 24, 30, [https://gibbs.science/efd/handouts/monin\\_obukhov\\_1954.pdf](https://gibbs.science/efd/handouts/monin_obukhov_1954.pdf), 1954.

732 Musial, W., Spitsen, P., Duffy, P., Beiter, P., Marquis, M., Hammond, R., and Shields, M.: *Offshore Wind Market*  
733 *Report: 2022 Edition*, NREL/TP-5000-83544, National Renewable Energy Laboratory, Golden, CO (United States),  
734 <https://doi.org/10.2172/188338>, 2022.

735 Nakanishi, M. and Niino, H.: An Improved Mellor–Yamada Level-3 Model: Its Numerical Stability and Application  
736 to a Regional Prediction of Advection Fog, *Boundary-Layer Meteorol*, 119, 397–407,  
737 <https://doi.org/10.1007/s10546-005-9030-8>, 2006.

738 Nilsen, T.: Icing believed to cause sinking of fishing boat in Barents Sea, 17 missing:  
739 <https://thebarentsobserver.com/en/2020/12/icing-believed-cause-sinking-fishing-boat-barents-sea-17-missing>, last  
740 access: 12 April 2023.

741 Niu, G.-Y., Yang, Z.-L., Mitchell, K. E., Chen, F., Ek, M. B., Barlage, M., Kumar, A., Manning, K., Niyogi, D.,  
742 Rosero, E., Tewari, M., and Xia, Y.: The community Noah land surface model with multiparameterization options  
743 (Noah-MP): 1. Model description and evaluation with local-scale measurements, *Journal of Geophysical Research:*  
744 *Atmospheres*, 116, <https://doi.org/10.1029/2010JD015139>, 2011.

745 Novacheck, J., Sharp, J., Schwarz, M., Donohoo-Vallett, P., Tzavelis, Z., Buster, G., and Rossol, M.: The Evolving  
746 Role of Extreme Weather Events in the U.S. Power System with High Levels of Variable Renewable Energy,  
747 NREL/TP-6A20-78394, 1837959, MainId:32311, NREL/TP-6A20-78394, 1837959, MainId:32311,  
748 <https://doi.org/10.2172/1837959>, 2021.



749 NREL: 2023 National Offshore Wind data set (NOW-23), <https://dx.doi.org/10.25984/1821404>, 2020.

750 Glossary - NOAA's National Weather Service: <https://w1.weather.gov/glossary/index.php?word=freezing+spray>,  
751 last access: 12 April 2023.

752 Nygaard, N. G.: Wakes in very large wind farms and the effect of neighbouring wind farms, *J. Phys.: Conf. Ser.*,  
753 524, 012162, <https://doi.org/10.1088/1742-6596/524/1/012162>, 2014.

754 Overland, J. E.: Prediction of Vessel Icing for Near-Freezing Sea Temperatures, *Weather and Forecasting*, 5, 62–77,  
755 [https://doi.org/10.1175/1520-0434\(1990\)005<0062:POVIFN>2.0.CO;2](https://doi.org/10.1175/1520-0434(1990)005<0062:POVIFN>2.0.CO;2), 1990.

756 Overland, J. E., Pease, C. H., Preisendorfer, R. W., and Comiskey, A. L.: Prediction of Vessel Icing, *Journal of*  
757 *Applied Meteorology and Climatology*, 25, 1793–1806, [https://doi.org/10.1175/1520-0450\(1986\)025<1793:POVI>2.0.CO;2](https://doi.org/10.1175/1520-0450(1986)025<1793:POVI>2.0.CO;2), 1986.

759 Parent, O. and Ilinca, A.: Anti-icing and de-icing techniques for wind turbines: Critical review, *Cold Regions*  
760 *Science and Technology*, 65, 88–96, <https://doi.org/10.1016/j.coldregions.2010.01.005>, 2011.

761 Platis, A., Siedersleben, S. K., Bange, J., Lampert, A., Bärfuss, K., Hankers, R., Cañadillas, B., Foreman, R.,  
762 Schulz-Stellenfleth, J., Djath, B., Neumann, T., and Emeis, S.: First in situ evidence of wakes in the far field behind  
763 offshore wind farms, *Sci Rep*, 8, 2163, <https://doi.org/10.1038/s41598-018-20389-y>, 2018.

764 Powers, J. G., Klemp, J. B., Skamarock, W. C., Davis, C. A., Dudhia, J., Gill, D. O., Coen, J. L., Gochis, D. J.,  
765 Ahmadov, R., Peckham, S. E., Grell, G. A., Michalakes, J., Trahan, S., Benjamin, S. G., Alexander, C. R., Dimego,  
766 G. J., Wang, W., Schwartz, C. S., Romine, G. S., Liu, Z., Snyder, C., Chen, F., Barlage, M. J., Yu, W., and Duda,  
767 M. G.: The Weather Research and Forecasting Model: Overview, System Efforts, and Future Directions, *Bulletin of*  
768 *the American Meteorological Society*, 98, 1717–1737, <https://doi.org/10.1175/BAMS-D-15-00308.1>, 2017.

769 Pronk, V., Bodini, N., Optis, M., Lundquist, J. K., Moriarty, P., Draxl, C., Purkayastha, A., and Young, E.: Can  
770 reanalysis products outperform mesoscale numerical weather prediction models in modeling the wind resource in  
771 simple terrain?, *Wind Energ. Sci.*, 7, 487–504, <https://doi.org/10.5194/wes-7-487-2022>, 2022.

772 Quint, D., Lundquist, J. K., Bodini, N., and Rosencrans, D.: Meteorological Impacts of Offshore Wind Turbines as  
773 Simulated in the Weather Research and Forecasting Model, *Wind Energy Science Discussions*, 1–34,  
774 <https://doi.org/10.5194/wes-2024-53>, 2024.

775 Rajewski, D. A., Takle, E. S., Lundquist, J. K., Oncley, S., Prueger, J. H., Horst, T. W., Rhodes, M. E., Pfeiffer, R.,  
776 Hatfield, J. L., Spoth, K. K., and Doorenbos, R. K.: Crop Wind Energy Experiment (CWEX): Observations of  
777 Surface-Layer, Boundary Layer, and Mesoscale Interactions with a Wind Farm, *Bulletin of the American*  
778 *Meteorological Society*, 94, 655–672, <https://doi.org/10.1175/BAMS-D-11-00240.1>, 2013.

779 Redfern, S., Optis, M., Xia, G., and Draxl, C.: Offshore wind energy forecasting sensitivity to sea surface  
780 temperature input in the Mid-Atlantic, *Wind Energy Science*, 8, 1–23, <https://doi.org/10.5194/wes-8-1-2023>, 2023.

781 Rosencrans, D., Lundquist, J. K., Optis, M., Rybchuk, A., Bodini, N., and Rossol, M.: Seasonal variability of wake  
782 impacts on US mid-Atlantic offshore wind plant power production, *Wind Energy Science*, 9, 555–583,  
783 <https://doi.org/10.5194/wes-9-555-2024>, 2024.

784 Ross, D. B. and Cardone, V.: Observations of oceanic whitecaps and their relation to remote measurements of  
785 surface wind Speed, *Journal of Geophysical Research (1896-1977)*, 79, 444–452,  
786 <https://doi.org/10.1029/JC079i003p00444>, 1974.

787 Russell, L. M.: Sea-spray particles cause freezing in clouds, *Nature*, 525, 194–195, <https://doi.org/10.1038/525194a>,  
788 2015.

789 Schneemann, J., Rott, A., Dörenkämper, M., Steinfeld, G., and Kühn, M.: Cluster wakes impact on a far-distant  
790 offshore wind farm's power, *Wind Energy Science*, 5, 29–49, <https://doi.org/10.5194/wes-5-29-2020>, 2020.

791 Shcherbina, A. Y. and Gawarkiewicz, G. G.: A coastal current in winter: 2. Wind forcing and cooling of a coastal  
792 current east of Cape Cod, *Journal of Geophysical Research: Oceans*, 113, <https://doi.org/10.1029/2008JC004750>,  
793 2008a.

794 Shcherbina, A. Y. and Gawarkiewicz, G. G.: A coastal current in winter: Autonomous underwater vehicle  
795 observations of the coastal current east of Cape Cod, *Journal of Geophysical Research: Oceans*, 113,  
796 <https://doi.org/10.1029/2007JC004306>, 2008b.

797 Siedersleben, S. K., Lundquist, J. K., Platis, A., Bange, J., Bärfuss, K., Lampert, A., Cañadillas, B., Neumann, T.,  
798 and Emeis, S.: Micrometeorological impacts of offshore wind farms as seen in observations and simulations,  
799 *Environ. Res. Lett.*, 13, 124012, <https://doi.org/10.1088/1748-9326/aaea0b>, 2018.

800 Stull B., R.: *An Introduction to Boundary Layer Meteorology*, Springer Science & Business Media,  
801 [https://books.google.com/books?hl=en&lr=&id=2PjrCAAAQBAJ&oi=fnd&pg=PR10&dq=An+Introduction+to+Bo](https://books.google.com/books?hl=en&lr=&id=2PjrCAAAQBAJ&oi=fnd&pg=PR10&dq=An+Introduction+to+Boundary+Layer+Meteorology+stull&ots=BdY_2W6EQ2&sig=eLIi5IVaua4aeHUWQt-NfG0IkTM#v=onepage&q=An%20Introduction%20to%20Boundary%20Layer%20Meteorology%20stull&f=false)  
802 [undary+Layer+Meteorology+stull&ots=BdY\\_2W6EQ2&sig=eLIi5IVaua4aeHUWQt-](https://books.google.com/books?hl=en&lr=&id=2PjrCAAAQBAJ&oi=fnd&pg=PR10&dq=An+Introduction+to+Boundary+Layer+Meteorology+stull&ots=BdY_2W6EQ2&sig=eLIi5IVaua4aeHUWQt-NfG0IkTM#v=onepage&q=An%20Introduction%20to%20Boundary%20Layer%20Meteorology%20stull&f=false)  
803 [NfG0IkTM#v=onepage&q=An%20Introduction%20to%20Boundary%20Layer%20Meteorology%20stull&f=false](https://books.google.com/books?hl=en&lr=&id=2PjrCAAAQBAJ&oi=fnd&pg=PR10&dq=An+Introduction+to+Boundary+Layer+Meteorology+stull&ots=BdY_2W6EQ2&sig=eLIi5IVaua4aeHUWQt-NfG0IkTM#v=onepage&q=An%20Introduction%20to%20Boundary%20Layer%20Meteorology%20stull&f=false),  
804 1988.

805 SWAN Team: *Scientific and Technical Documentation (SWAN Cycle III version 41.31A)*, Delft University of  
806 Technology, <https://swanmodel.sourceforge.io/download/zip/swantech.pdf>, 2020.

807 Tewari, M., Chen, F., Wang, W., Dudhia, J., LeMone, M., Mitchell, K., Ek, M., Gayno, G., Wegiel, J., and Cuenca,  
808 R. H.: (PDF) Implementation and verification of the united NOAH land surface model in the WRF model,  
809 *Proceedings of the 20th conference on weather analysis and forecasting/16th conference on numerical weather*  
810 *prediction*, 14,  
811 [https://www.researchgate.net/publication/286272692\\_Implementation\\_and\\_verification\\_of\\_the\\_united\\_NOAH\\_land](https://www.researchgate.net/publication/286272692_Implementation_and_verification_of_the_united_NOAH_land_surface_model_in_the_WRF_model)  
812 [\\_surface\\_model\\_in\\_the\\_WRF\\_model](https://www.researchgate.net/publication/286272692_Implementation_and_verification_of_the_united_NOAH_land_surface_model_in_the_WRF_model), 2004.

813 Thompson, G., Field, P. R., Rasmussen, R. M., and Hall, W. D.: Explicit Forecasts of Winter Precipitation Using an  
814 Improved Bulk Microphysics Scheme. Part II: Implementation of a New Snow Parameterization, *Monthly Weather*  
815 *Review*, 136, 5095–5115, <https://doi.org/10.1175/2008MWR2387.1>, 2008.

816 Tolman, H., Abdolali, A., Accensi, M., Alves, J.-H., Arduin, F., Babanin, A., Barbariol, F., Benetazzo, A., Bidlot,  
817 J., Booij, N., Boutin, G., Bunney, C., Campbell, T., Chalikov, D., Chawla, A., Cheng, S., Collins III, C., Filipot, J.-  
818 F., Flampouris, S., and Liang, Z.: User manual and system documentation of WAVEWATCH III (R) version 6.07,  
819 [https://www.researchgate.net/publication/336069899\\_User\\_manual\\_and\\_system\\_documentation\\_of\\_WAVEWATCH](https://www.researchgate.net/publication/336069899_User_manual_and_system_documentation_of_WAVEWATCH_H_III_R_version_607)  
820 [H\\_III\\_R\\_version\\_607](https://www.researchgate.net/publication/336069899_User_manual_and_system_documentation_of_WAVEWATCH_H_III_R_version_607), 2019.

821 Tomaszewski, J. M. and Lundquist, J. K.: Simulated wind farm wake sensitivity to configuration choices in the  
822 *Weather Research and Forecasting model version 3.8.1*, *Geoscientific Model Development*, 13, 2645–2662,  
823 <https://doi.org/10.5194/gmd-13-2645-2020>, 2020.

824 U.S. Navy: *U. S. Navy Cold Weather Handbook for Surface Ships*, Surface Ship Survivability Office,  
825 [https://media.defense.gov/2021/Feb/25/2002588484/-1/-1/0/CG%20070%20-](https://media.defense.gov/2021/Feb/25/2002588484/-1/-1/0/CG%20070%20-%20US%20NAVY%20COLD%20WEATHER%20HANDBOOK.PDF)  
826 [%20US%20NAVY%20COLD%20WEATHER%20HANDBOOK.PDF](https://media.defense.gov/2021/Feb/25/2002588484/-1/-1/0/CG%20070%20-%20US%20NAVY%20COLD%20WEATHER%20HANDBOOK.PDF), 1988.

827 Vavrus, S., Walsh, J. E., Chapman, W. L., and Portis, D.: The behavior of extreme cold air outbreaks under  
828 greenhouse warming, *International Journal of Climatology*, 26, 1133–1147, <https://doi.org/10.1002/joc.1301>, 2006.

829 Wallace, J. M. and Hobbs, P. V.: *Atmospheric Science: An Introductory Survey*, 2nd ed., Elsevier, University of  
830 Washington, ISBN:978-0-12-732951-2, 2006.

831 Wei, K., Yang, Y., Zuo, H., and Zhong, D.: A review on ice detection technology and ice elimination technology for  
832 wind turbine, *Wind Energy*, 23, 433–457, <https://doi.org/10.1002/we.2427>, 2020.

833 Winters, A. C., Bosart, L. F., and Keyser, D.: Antecedent North Pacific Jet Regimes Conducive to the Development  
834 of Continental U.S. Extreme Temperature Events during the Cool Season, *Weather and Forecasting*, 34, 393–414,  
835 <https://doi.org/10.1175/WAF-D-18-0168.1>, 2019.

836 Xia, G., Zhou, L., Freedman, J. M., Roy, S. B., Harris, R. A., and Cervarich, M. C.: A case study of effects of  
837 atmospheric boundary layer turbulence, wind speed, and stability on wind farm induced temperature changes using  
838 observations from a field campaign, *Clim Dyn*, 46, 2179–2196, <https://doi.org/10.1007/s00382-015-2696-9>, 2016.

839  
840